การคำนวณการไหลที่มีพื้นผิวอิสระภายใต้อิทธิพลของการกระจายความดัน
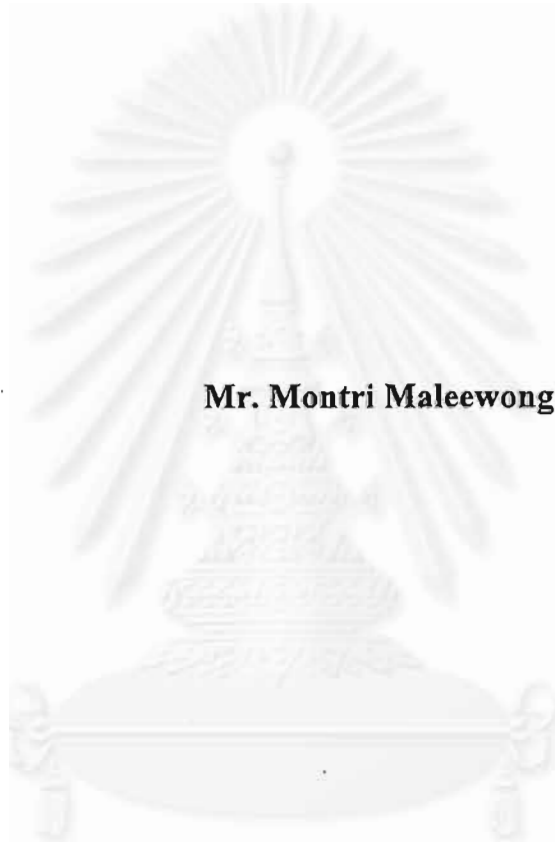
นายมนตรี มาลีวงศ์

ลิขสิทธิ์ของ จุฬาลงกรณ์มหาวิทยาลัย

I18710049

COMPUTATION OF FREE-SURFACE FLOWS UNDER
THE INFLUENCE OF PRESSURE DISTRIBUTION

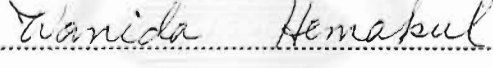**Mr. Montri Maleewong**

Thesis Title   COMPUTATION OF FREE-SURFACE FLOWS UNDER THE
INFLUENCE OF PRESSURE DISTRIBUTION
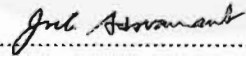
By   Mr. Montri Maleewong
Department   Mathematics
Thesis Advisor   Assist. Prof. Dr. Jack Asavanant
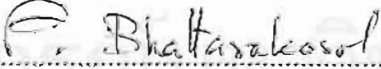
Accepted by the Faculty of Science, Chulalongkorn University in Partial
Fulfillment of the Requirements for the Master's Degree

.... Dean of Faculty of Science

(Assoc. Prof. Dr. Wanchai Phothiphichitr)

THESIS COMMITTEE

.... Chairperson

(Assoc. Prof. Dr. Wanida Hemakul)

.... Thesis Advisor

(Assist. Prof. Dr. Jack Asavanant)

.... Member

(Assist. Prof. Dr. Pattarasinee Bhattarakosol)

มนตรี มาลีวงศ์ : การคำนวณการไหลที่มีพื้นผิวอิสระภายใต้อิทธิพลของการกระจายความ
ดัน (COMPUTATION OF FREE-SURFACE FLOWS UNDER THE INFLUENCE OF
PRESSURE DISTRIBUTION) อาจารย์ที่ปรึกษา :
ผศ. ดร. จักษ์ อัศวานันท์ ; 92 หน้า. ISBN 974-333-418-1.

เราพิจารณาการไหลใน 2 มิติ ที่เป็นอิสระจากเวลา ภายใต้การกระจายความดัน ในน้ำที่มี
ความลึกจำกัด แรงโน้มถ่วงของโลกได้ถูกกำหนดในเงื่อนไขขอบเขต ปัญหานี้แก้โดยวิธีเชิงตัวเลข
boundary integral equation เราได้แสดงว่าทั้ง supercritical flow และ subcritical flow คำตอบ
ขึ้นอยู่กับพารามิเตอร์ 3 ตัว คือ (i) Froude number (ii) ขนาดของการกระจายความดัน และ (iii)
ช่วงความกว้างของการกระจายความดัน สำหรับกรณีของ supercritical flows คำตอบมี 2 คำตอบ
ที่สอดคล้องกันที่ค่า Froude number ค่าเดียวกันเมื่อความดันมีค่าเป็นบวก และคำตอบมีเพียงคำ
ตอบเดียวเมื่อความดันมีค่าเป็นลบ สำหรับกรณีของ subcritical flows คำตอบจะมีคลื่นที่เกิดด้าน
หลังของการกระจายความดัน ขณะที่ค่า Froude number ลดลง คลื่นเหล่านี้จะหายไปเมื่อค่า
Froude number เข้าใกล้ค่าวิกฤต เราได้ตรวจสอบผลของแรงตึงผิวในกรณีของ subcritical
symmetric flows ด้วย เราพบว่าสำหรับค่าของ Bond number บางค่า และความดันมีค่าเป็นบวก
จะเกิดรูปแบบจำกัดที่มี trapped bubble เมื่อค่า Froude number เข้าใกล้ค่าวิกฤต (ใกล้ค่าศูนย์)
ในทางตรงข้าม พื้นผิวอิสระมีแนวโน้มที่จะเกิด inflexion points จำนวนมากเมื่อค่า Froude
number เข้าใกล้ค่า 1

ภาควิชา   คณิตศาสตร์   ลายมือชื่อนิสิต _____
สาขาวิชา   วิทยาการคณนา   ลายมือชื่ออาจารย์ที่ปรึกษา _____
ปีการศึกษา   2542   ลายมือชื่ออาจารย์ที่ปรึกษาร่วม _____

       Steady two-dimensional flows due to an applied pressure distribution in water
of finite depth are considered. Gravity is included in the dynamic boundary condition.
The problem is solved numerically by using the boundary integral equation technique.
It is shown that, for both supercritical and subcritical flows, solutions are
characterized by three parameters: (i) the Froude number, (ii) the magnitude of
applied pressure distribution and (iii) the span length of applied pressure distribution.
For supercritical flows, there exist up to two solutions corresponding to the same
value of Froude number for positive pressures and a unique solution for negative
pressures. For subcritical flows, there are solutions with wave behind the applied
pressure distribution. As the Froude number decreases, these waves diminish when
the Froude numbers approach the critical values. The surface tension effect is also
investigated in the case of subcritical symmetric flows. It is found that for some
values of the Bond number and positive pressures, there exist limiting configurations
with trapped bubble as the Froude number approaches a critical value (near zero). On
the other hand, the free surface profile tends to develop a large number of inflexion
points as the Froude numbers approach 1.

ภาควิชา ....คณิตศาสตร์.......... ลายมือชื่อนิสิต ....

สาขาวิชา ....วิทยาการคณนา...... ลายมือชื่ออาจารย์ที่ปรึกษา ....

ปีการศึกษา ....2542................ ลายมือชื่ออาจารย์ที่ปรึกษาร่วม ....

Acknowledgments

Contents

Chapter 1
Introduction

Efforts to analyze the hydrodynamical characteristics of free-surface flow with surface-disturbance have been divided primarily between theoretical and experimental considerations. There are various types of surface-disturbance occurred in nature and some are due to man-made structures. Most of the theoretical studies lie mainly in the two-dimensional framework and were based on global analysis. Results from the laboratory experiments provides, on the other hand, small scale analysis for both two- and three- dimensional problems.

We devote this research to the investigations of steady two-dimensional potential flow of an inviscid and incompressible fluid due to pressure distribution. These two-dimensional models allow us to utilize various mathematical tools for solving the problem, for example, the use of complex analysis particularly conformal transformation. This simplification will not only provide qualitative behaviors but also give some insights to the real flow situations. Though the assumption of steadiness may seem unreal but we can always choose the appropriate moving frame of reference in such a way that the flow becomes steady.

In this study, we consider fully nonlinear free-surface flow past an applied pressure distribution on the free surface. The fluid domain is of finite depth with no vertical boundaries in the far fields. Such flows can be produced by blowing air onto the surface of water flowing in a channel with parallel sidewalls. In the far field on upstream, the flow is assumed to approach a uniform stream with constant velocity U and uniform depth H. The flow is characterized by a nondimensional parameter, the Froude number,

$$F = \frac{U}{\sqrt{gH}} , \qquad\qquad (1.1)$$

where g denotes the acceleration of gravity.

In general, this flow configuration can be served as a model of moving vehicles such as hovercraft in a long canal. It may also be viewed as an inverse method of solution to the classical ship-wave problem. When the pressure distribution is applied, the free surface will deform in some manner that must be determined as part of the solution. The portion of the deformed free surface at which the pressure distribution is applied can be viewed as a rigid obstacle. It can be possible to find solutions for flow past different classes of hull forms corresponding to the pressure distribution problem.

It has been known that, problems in free-surface hydrodynamics under the influence of gravity are too difficult to solve exactly. Appropriate techniques of mathematical approximations are usually sought. Here, we introduce the integral equation formulation based on analytic function theory which may prove useful in treating variety of fluid flow problems with free boundaries. Numerical results can be obtained from this method after a few Newtonian iterations.

The problem of free surface pressure distributions has been studied quite extensively in the case of infinite depth for over 150 years. The classical linearized version of the two-dimensional problem was solved long ago and was discussed in detail by Lamb (1932). It was shown that for some pressure distributions the motion is drag-free. That is, the free surface is symmetric with respect to the applied pressure distribution without a train of sinusoidal waves in the far field. Schwartz (1981) reformulated the problem into a boundary integral equation and solved numerically. He showed that, for some values of the Froude number (defined by using the span length of the pressure distribution as the length scale), nonlinear theory gave drag-free solution while linearized

2

theory did not. He also found nonlinear wave train in the form of narrow crests an broad troughs which were essentially periodic and propagated downstream.

In the case of finite depth, Von-Kerczek and Salvesen (1977) placed a network of mesh points over the entire flow domain and performed finite difference calculations (successive overrelaxation) to obtain nonlinear solutions. Their numerical calculations were restricted to certain values of the ratio of pressure-distribution-length to the depth of the flow domain. The nonlinear wave train propagates downstream while the flow satisfies radiation condition on the upstream free surface. They found that, the effect of the nonlinearities can clearly be seen on the phase shift in the solutions.

This thesis is organized in two folds. Firstly, the effect of gravity is introduced to the flow field. This problem is studied thoroughly in chapters 2 and 3. Secondly, the combined effects of gravity and surface tension are investigated in chapter 4. We consider the fluid domain of finite depth. The conditions of incompressibility and irrotationality of the fluid motion imply the existence of the potential function and the stream function. The fluid domain in the physical plane is transformed onto the complex plane. Bernoulli equation is applied on the free surface while we assume no flow across the bottom boundary. We satisfy the bottom conditon by using Schwartz reflection principle. We solve the problem numerically by the boundary integral equation method based on Cauchy's integral formula. The integral equation is derived to obtain a relationship of the flow variables at the free surface only. Thus mesh points in the numerical scheme need only be placed at the free surface rather than throughout the entire fluid. We obtain the numerical solutions by solving a system of nonlinear algebraic equations on the free surface using Newton's Method. Details of the formulation and the numerical procedure are given in chapter 2.

In chapter 3, we present and discuss numerical results for two flow regimes:

3

supercritical flow $F > 1$ and subcritical flow $F < 1$. As we shall see, both supercritical flows and subcritical flows are characterized by three parameters. These parameters are (i) the Froude number F, (ii) the magnitude of applied pressure distribution ϵ (positive pressure if $\epsilon > 0$ and negative pressure if $\epsilon < 0$), (iii) the span length of pressure distribution. In section 3.1, we present the numerical results of supercritical flows. Our results show that the free surface profile is always symmetric (drag free) with respect to the axis of symmetry of the pressure distribution. There are two different families of solutions when $\epsilon > 0$. One family is a purturbed solution of uniform stream whereas the other is a purturbed solution of solitary wave. When $\epsilon < 0$, there is only one family of solutions that exists for all values of Froude number up to unity. We expect that these solutions can be extend to the subcritical regime ($F < 1$) by allowing waves downstream. The case of subcritical flows is discussed in section 3.2. The solutions are characterized by a train of nonlinear waves downstream while the flow satisfies the radiation condition on the upstream. As F decreases, there are critical values of Froude number at which the flows become drag free. Our finding is in contrast with the problem of flows past a surface-piercing object. Asavanant and Vanden-Broeck (1994) showed that subcritical flows past a parabolic-shaped object never possess drag-free solutions but they will always approach Stokes' limiting configuration. Difficulty in the numerical process occurs when the Froude number is increasing to unity from below because of the unpredicted numerical disturbances in periodic forms on the upstream free surface. This has sabotaged the convergence of the numerical scheme. However we conjecture that, for subcritical solutions, the wave length would approach infinity as $F \uparrow 1$ and would extend to the supercritical regime.

The importance of surface tension effects on gravity waves is discussed in chapter 4. We include the effects of both gravity and surface tension in the dynamic boundary condition on the free surface. At this early stage of our

4

study, we shall restrict ourselves in the case of subcritical symmetric flows due to pressure distribution. We solve the problem numerically by the boundary integral equation method for arbitrary values of the Froude number, magnitude of pressure distribution, span length of pressure distribution and Bond number τ^* (which is the nondimensional parameter including gravity and surface tension effects). Our numerical results show that, for a fixed value of τ^* and $\epsilon > 0$, there are two families of solutions. One family of solutions is a purturbed solution of uniform stream whereas the other is a purturbed solution of solitary wave. When $\epsilon > 0$ and $\tau^* < \frac{1}{2}$, the perturbed solution of solitary wave approaches a limiting configuration with trapped bubble as F close to 0. Moreover, when $\epsilon > 0$ and $\tau^* < \frac{1}{3}$, we found that the free surface profile develops a large number of inflexion points as τ^* decreases. These solutions are found to be qualitatively similar to those gravity-capillary solitary wave in water of finite depth (Hunter and Vanden-Broeck, 1983). We have shown in section 4.2 that more solutions can be obtained when there is an applied pressure distribution in comparison with their results.

Chapter 2

Formulation of Flows with Gravity

2.1 Formulation

We consider the steady two-dimensional, irrotational flow of an inviscid incompressible flow in the domain bounded below by a rigid bottom and above by a free surface as shown in Figure 2.1. We choose Cartesian coordinates with the x-axis along the free surface at $x = -\infty$ and the y-axis directed vertically upwards through the symmetry line of the applied pressure distribution. Gravity is acting in the negative y- direction. The velocity components in the x- and y- directions are denoted by u and v respectively. As $x \to -\infty$, the flow is assumed to approach a uniform stream with constant velocity U and uniform depth H.

Let us introduce dimensionless variables by choosing U as the unit velocity and H as the unit depth. The conditions of incompressibility and irrotationality of the fluid motion imply the existence of the potential function $\phi(x,y)$ and the stream function $\psi(x,y)$. We define the complex potential $f(z) = \phi(x,y) + i\psi(x,y)$ and the complex velocity $\zeta = \frac{df}{dz} = u - iv$ where $z = x + iy$. Both f and ζ are analytic functions of z. Without loss of generality we choose $\psi = 0$ on the free surface and the bottom defines another streamline on which $\psi = -UH$. By the choice of our dimensionless variables we will have $\psi = -1$ on the bottom (see Figure 2.2). The flow domain in the complex f -plane is simply an infinite strip defined by $D = \{(\phi,\psi)| -\infty < \phi < \infty, -1 < \psi < 0\}$.
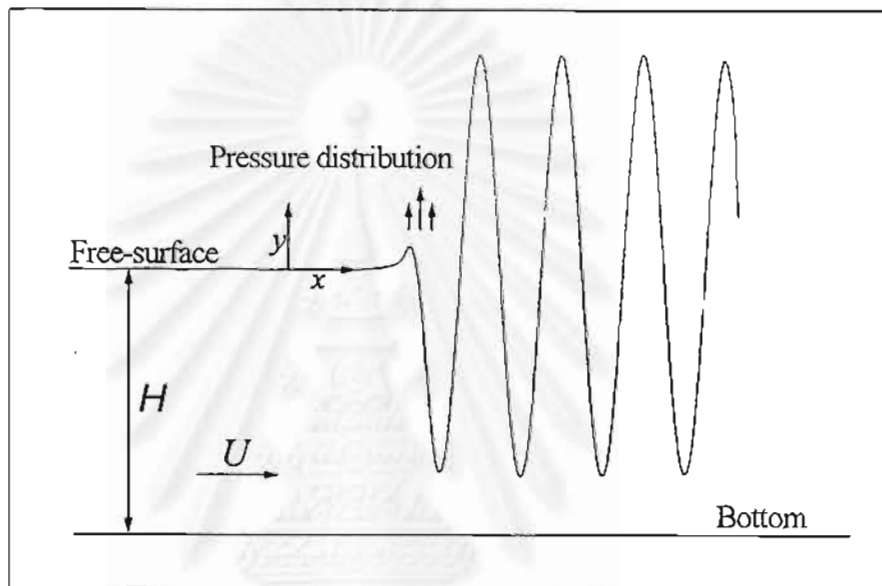
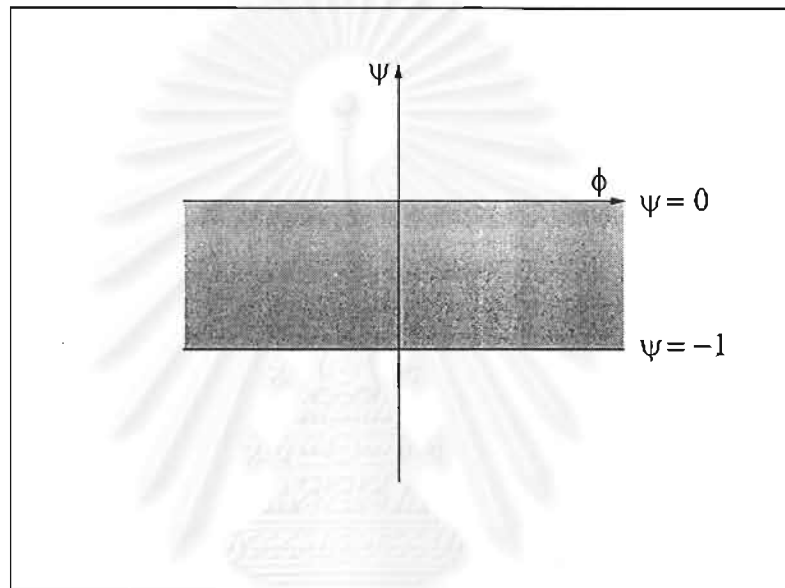Figure 2.1: Sketch of flow domain under the applied pressure distribution between C and D.

Figure 2.2: The complex f- plane by the transformation $f = \phi + i\psi$.

The nonlinear free-surface condition for this problem can be expressed by the Bernoulli equation

$$\frac{1}{2}q^2 + gy + \frac{p}{\rho} = \text{constant on the free surface} \qquad (2.1)$$

where q, p and ρ denote the magnitudes of the fluid velocity, the pressure and the fluid density respectively. Here g is the acceleration of gravity. We determine the constant term on the right hand side of (2.1) by using flow condition in the far field, i.e., $x \to -\infty$. That is,

$$\frac{1}{2}q^2 + gy + \frac{p}{\rho} = \frac{1}{2}U^2 + \frac{p_0}{\rho}$$

Here p_0 represents the atmospheric pressure which is constant along the free surface. Putting $q' = \frac{q}{U}$ and $y' = \frac{y}{H}$, we have

$$\frac{1}{2}(q'U)^2 + gHy' + \frac{1}{\rho}(p - p_0) = \frac{1}{2}U^2$$

$$q'^2 + 2\frac{gH}{U^2}y' + \frac{2}{\rho U^2}(p - p_0) = 1$$

$$q^2 + \frac{2}{F^2}y + \bar{p} = 1 \qquad (2.2)$$

Eq.(2.2) is the dimensionless form of Bernoulli equation where $\bar{p} = \frac{(p-p_0)}{\frac{1}{2}\rho U^2}$ and F is the Froude number defined in (1.1). The kinematic condition on the bottom is

$$v(\phi, \psi) = 0 \text{ on } \psi = -1 \qquad (2.3)$$

We now define the analytic function $\xi = u - iv - 1$ in the domain D. Here ξ is real on the bottom boundary $\psi = -1$. By the Schwartz reflection principle we can satisfy the kinematic condition (2.3) on the bottom by reflecting the flow field in the physical z- plane about the line $y = -H$. Let Ω and $\overline{\Omega}$ denote the fluid domain in the z- plane and its reflection. The function ξ can be extended to a function Ξ which is analytic in $\Omega \cup \overline{\Omega}$ and is defined as

$$\Xi(z) = \begin{cases} \overline{\xi(\bar{z})} & : \quad z \in \overline{\Omega} \\ \xi(z) & : \quad z \in \Omega \end{cases}$$

9

The overbar represents the complex conjugation of the function. Applying the Cauchy integral formula to the function Ξ in the extended region in the f-plane, which is the strip $-2 \leq \psi \leq 0$, we obtain

$$\Xi = u - iv - 1 = -\frac{1}{2\pi i} \oint_\Gamma \frac{u(f') - iv(f') - 1}{f' - f} df' \qquad (2.4)$$

Here Γ is the negatively oriented contour given (see Figure 2.3) by

$$\Gamma = \begin{cases} \Gamma_1 : f' = \phi' & ; \quad -R' \leq \phi' \leq R' \\[2mm] \Gamma_2 : f' = R' + i\psi' & ; \quad -2 \leq \psi' \leq 0 \\[2mm] \Gamma_3 : f' = \phi' - 2i & ; \quad -R' \leq \phi' \leq R' \\[2mm] \Gamma_4 : f' = -R' + i\psi' & ; \quad -2 \leq \psi' \leq 0 \end{cases}$$

Letting f approaches the boundary $\psi = 0$, we obtain

$$\Xi(\phi, 0) = u(\phi, 0) - iv(\phi, 0) - 1 = -\frac{1}{\pi i} \oint_\Gamma \frac{u(f') - iv(f') - 1}{f' - \phi} df' \qquad (2.5)$$

We denote by $u(\phi)$ and $v(\phi)$ the velocity components in the x- and y- directions on the free surface $\psi = 0$. From (2.5), we have

$$
\begin{aligned}
u(\phi) - iv(\phi) - 1 = {} & -\frac{1}{\pi i} \int_{-R'}^{R'} \frac{u(\phi') - iv(\phi') - 1}{\phi' - \phi} d\phi' \\[2mm]
& + \frac{1}{\pi i} \int_{-R'}^{R'} \frac{u(\phi' - 2i) - iv(\phi' - 2i) - 1}{\phi' - 2i - \phi} d(\phi' - 2i) \\[2mm]
& + \frac{1}{\pi i} \int_{-2}^{0} \frac{u(R' + i\psi') - iv(R' + i\psi') - 1}{(R' + i\psi') - \phi} d(R' + i\psi') \\[2mm]
& - \frac{1}{\pi i} \int_{-2}^{0} \frac{u(-R' + i\psi') - iv(-R' + i\psi') - 1}{(-R' + i\psi') - \phi} d(-R' + i\psi')
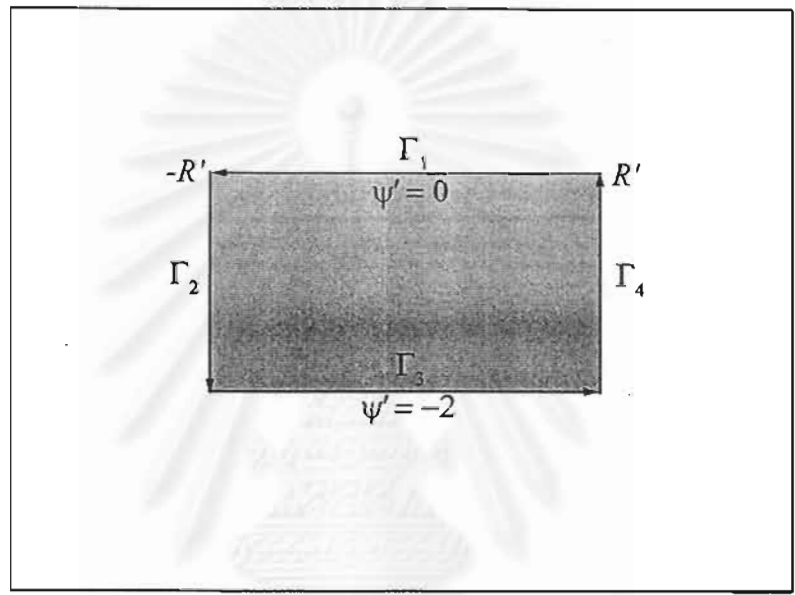\end{aligned}
$$

$$(2.6)$$

Figure 2.3: The path of negatively oriented contour integral Γ.

One can easily verify that the last two integrals on the right hand side of (2.6) vanish as $R' \to \infty$. To show this, we consider the third term on this equation.

$$\frac{1}{\pi i} \int_{-2}^{0} \frac{u(R' + i\psi') - iv(R' + i\psi') - 1}{(R' + i\psi') - \phi} d(R' + i\psi')$$

$$= \frac{1}{\pi} \int_{-2}^{0} \frac{u(R' + i\psi') - iv(R' + i\psi') - 1}{(R' - \phi) + i\psi'} d\psi'$$

$$= \frac{1}{\pi} \int_{-2}^{0} \frac{u(R' + i\psi') - iv(R' + i\psi') - 1}{(R' - \phi) + i\psi'} \cdot \frac{(R' - \phi) - i\psi'}{(R' - \phi) - i\psi'} d\psi'$$

$$= \frac{1}{\pi} \int_{-2}^{0} \frac{(u(R' + i\psi') - iv(R' + i\psi') - 1)((R' - \phi) - i\psi')}{(R' - \phi)^2 + \psi'^2} d\psi'$$

We can see that order of the above equation is $1/R'$. Let $z' = R' + i\psi'$. Since u and v are bounded functions in the flow domain and $u(z') \to 1$ and $v(z') \to 0$ as $R' \to \infty$, it then follows that

$$\lim_{R' \to \infty} \frac{1}{\pi i} \int_{-2}^{0} \frac{u(R' + i\psi') - iv(R' + i\psi') - 1}{(R' + i\psi') - \phi} d(R' + i\psi') = 0$$

Similarly, the fourth term on the right hand side of (2.6) can be shown that

$$\lim_{R' \to \infty} \frac{1}{\pi i} \int_{-2}^{0} \frac{u(-R' + i\psi') - iv(-R' + i\psi') - 1}{(-R' + i\psi') - \phi} d(-R' + i\psi') = 0$$

Taking limit as $R' \to \infty$, (2.6) yields

$$u(\phi) - iv(\phi) - 1 = -\frac{1}{\pi i} \int_{-\infty}^{\infty} \frac{u(\phi') - iv(\phi') - 1}{\phi' - \phi} d\phi' + \frac{1}{\pi i} \int_{-\infty}^{\infty} \frac{\overline{u}(\phi') - i\overline{v}(\phi') - 1}{\phi' - 2i - \phi} d\phi'$$

(2.7)

where $\overline{u}(\phi')$ and $\overline{v}(\phi')$ represent the horizontal and vertical components of the velocity on the image $\psi = -2$ of the free surface. We can simplify (2.7) by

using elementary complex analysis, as follows

$$u(\phi) - iv(\phi) - 1 = -\frac{1}{\pi i} \int\limits_{-\infty}^{\infty} \frac{u(\phi') - iv(\phi') - 1}{\phi' - \phi} d\phi'$$

$$+ \frac{1}{\pi i} \int\limits_{-\infty}^{\infty} \frac{(\overline{u}(\phi') - 1) - i\overline{v}(\phi')}{(\phi' - \phi) - 2i} \cdot \frac{(\phi' - \phi) + 2i}{(\phi' - \phi) + 2i} d\phi'.$$

From the fact that $v(\phi') = -\overline{v}(\phi')$ and $u(\phi') = \overline{u}(\phi')$, we can relate the integral over the reflection of the free surface to the integral over the free surface itself. Finally, after taking the real parts, we can rewrite (2.7) as

$$u(\phi) - 1 = \frac{1}{\pi} \int\limits_{-\infty}^{\infty} \frac{v(\phi')}{\phi' - \phi} d\phi' + \frac{1}{\pi} \int\limits_{-\infty}^{\infty} \frac{v(\phi')(\phi' - \phi) + 2(u(\phi') - 1)}{(\phi' - \phi)^2 + 4} d\phi' \quad (2.8)$$

Using the identity

$$\frac{\partial x}{\partial \phi} + i\frac{\partial y}{\partial \phi} = \frac{1}{u - iv}, \quad (2.9)$$

the Bernoulli equation (2.2) can be written in terms of $u(\phi)$ and $v(\phi)$ as

$$u^2(\phi) + v^2(\phi) + \frac{2}{F^2} \int\limits_{-\infty}^{\phi} \frac{v(\phi')}{u^2(\phi') + v^2(\phi')} d\phi' + \tilde{p} = 1 \; ; -\infty < \phi < \infty \quad (2.10)$$

We consider now that the distribution of pressure be described by function with compact support defined by

$$\tilde{p} = \begin{cases} 0 & , \; for \; |\phi| > \phi_0 \\ \epsilon e^{\frac{1}{|\frac{\phi}{\phi_0}|^2 - 1}} & , \; for \; |\phi| < \phi_0 \end{cases}$$

where ϕ_0 is the value of potential function ϕ on the free surface. The problem becomes that of finding $u(\phi)$ and $v(\phi)$ satisfying (2.8) and (2.10). The shape of the unknown free surface can be determined by numerically integrating the identity (2.9).

13

2.2 Numerical Procedure

To obtain nonlinear solution of (2.8) and (2.10) in the previous section, it is necessary to resort to a numerical method. We solve this system of integral equations by discretizing the free surface in the f- plane. Thus we introduce the M mesh points.

$$\phi_i = (i - 1)E, \quad i = 1, 2, ..., M \tag{2.11}$$

where E is the discretization interval. The values of $u(\phi)$ and $v(\phi)$ are computed at the mid points

$$\phi_{i+\frac{1}{2}} = \frac{\phi_i + \phi_{i+1}}{2}, \quad i = 1, 2, ..., M - 1$$

Equation (2.8) and (2.10) are to be satisfied at these mid points. We denote the value of u and v at the mesh points by u_i and v_i. The integral in (2.8) are truncated downstream at the point ϕ_M subject to the requirement that the pressure distribution is applied on the free surface sufficiently far from the end points. The error due to this truncation can be estimated by comparing the solutions for different values of M and E.

We approximate the integral in (2.8) by using the trapezoidal rule with summation over ϕ_i. Since the spacing points are symmetric with respect to the pole, the singularity is subtracted from the Cauchy principal-value integral leaving nonsingular integrals (see Appendix). Next we replace (2.8) by

$$u_{i+\frac{1}{2}} - 1 = \frac{1}{\pi} \int_{\phi_1}^{\phi_M E} v_i \left[\frac{1}{\phi' - \phi_{i+\frac{1}{2}}} \right] d\phi' + \frac{1}{\pi} \int_{\phi_1}^{\phi_M E} \frac{v_i(\phi' - \phi_{i+\frac{1}{2}}) + 2(u_i - 1)}{(\phi' - \phi_{i+\frac{1}{2}})^2 + 4} \, d\phi' \tag{2.12}$$

The radiation condition $v \to 0$ as $\phi \to -\infty$ is now applied at the first mesh point ϕ_1, i.e.,

$$v_1 = 0 \tag{2.13}$$

The Bernoulli equation (2.10) is satisfied at the mesh points

$$u_i^2 + v_i^2 + \frac{2}{F'^2} y_i + \tilde{p}_i = 1; \quad i = 1, 2, 3, ..., M \tag{2.14}$$

We obtain $2M$ equations from (2.12) - (2.14) for the $2M$ unknows u_i and v_i. It is convenient to write this system of equations in the form

$$f_i(\eta_1, \eta_2, ..., \eta_{2M}) = 0; \quad i = 1, 2, ..., 2M \tag{2.15}$$

where $\{\eta_j\}_{j=1}^{M} = \{u_j\}_{j=1}^{M}$ and $\{\eta_j\}_{j=M+1}^{2M} = \{v_j\}_{j=1}^{M}$.

We solve (2.15) by Newton's method . Thus if $\eta_j^{(k)}$ is an approximation to the solution, the next approximation $\eta_j^{(k+1)}$ is obtained by

$$\eta_j^{(k+1)} = \eta_j^{(k)} - \Delta_j^{(k)}; \quad j = 1, 2, ..., 2M \tag{2.16}$$

where the corrections $\Delta_j^{(k)}$ are calculated from

$$\sum_{j=1}^{2M} \left[\frac{\partial f_i}{\partial \eta_j} \right]^{(k)} \Delta_j^{(k)} = f_i^{(k)}; \quad i = 1, 2, ..., 2M \tag{2.17}$$

The Jacobians $\frac{\partial f_i}{\partial \eta_j}$ are determined by exact differentiation of (2.15).

To conclude this section, let us define a span length L of the pressure distribution by

$$L = 2 \int_0^{\phi_0} \frac{\partial x}{\partial \phi} \, d\phi \tag{2.18}$$

The numerical scheme developed in this section is used to calculate solutions for various values of F^2, ϵ and L. As we shall see later, there are two-parameter family of solutions. Furthermore, it is found that the behaviors of solution for different values of L are quanlitatively similar. Thus it suffices to obtain computed solutions for various values of F^2 and ϵ with L fixed. The numerical accuracy is checked by increasing M while keeping E fixed and vice versa.

Chapter 3

Numerical Results of Flows with Gravity

We use the numerical scheme described in the previous chapter to compute solutions for two flow regimes: supercritical flow $F > 1$ and subcritical flow $F < 1$. In section 3.1, we present and discuss numerical results of supercritical flows. Our numerical results show that the flow is always symmetric with respect to the axis of symmetry of the pressure distribution. Two families of solutions are found when $\epsilon > 0$ (see Figure 3.5). One family is a perturbed solution of uniform stream, whereas the other is a perturbed solution of a solitary wave. When $\epsilon < 0$, there is only one family of supercritical-flow solutions that exist for all values of Froude number up to unity (see Figure 3.9). The case of subcritical flows is discussed in section 3.2. A train of nonlinear waves is generated behind the applied pressure distribution. There are critical values of Froude number at which the wave amplitude diminishes. This is the so-called "drag-free" solution. Our finding is in contrast with the problem of flows past a surface-piercing object. Asavanant and Vanden-Broeck (1994) showed that subcritical flows past a parabolic-shaped object never possess drag-free solutions but they always approach Stokes' limiting configuration.

3.1   Supercritical Flow

As Mentioned in section 2.2, we calculate solutions of the system of nonlinear algebraic equations (2.12)-(2.14) for various values of F^2, ϵ and L. It is found that the behaviors of solutions for different values of L are qualitatively similar. This is illustrated in Figure 3.1-3.4. Thus it is sufficient to present the results for a given value of L. We therefore set $L = 3.0$ throughout the calculation of
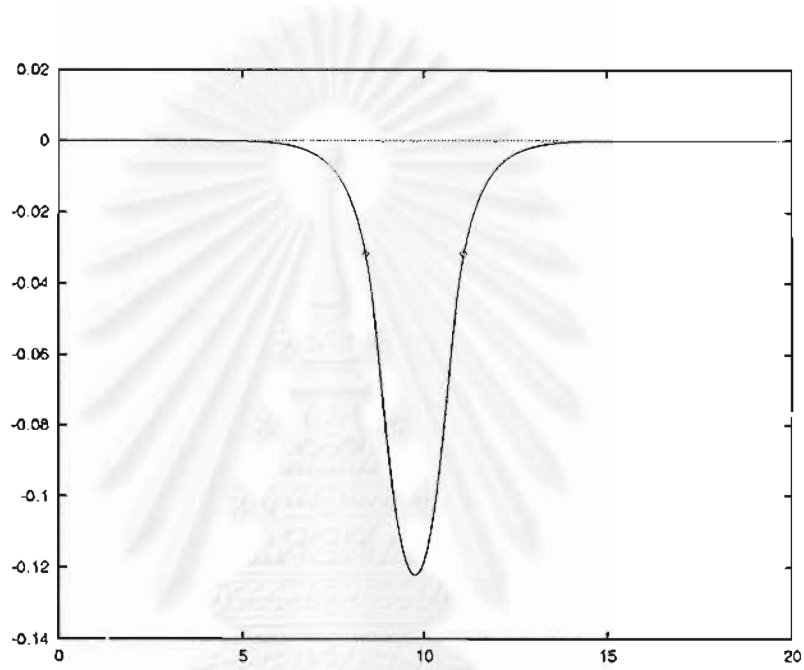
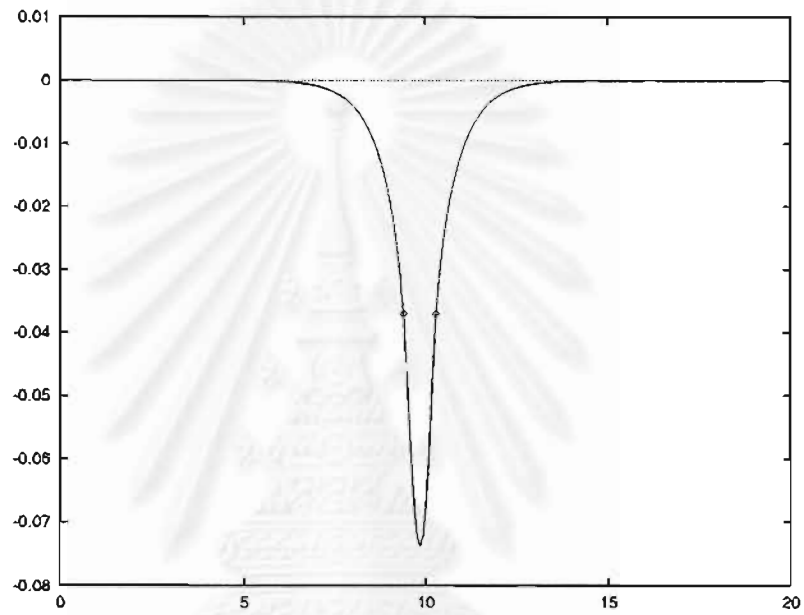Figure 3.1: Typical free-surface profile for $L = 3.0, F^2 = 10.0, \epsilon = -1.0$ and $E = 0.15$.

Figure 3.2: Typical free-surface profile for $L = 1.0, F^2 = 10.0, \epsilon = -1.0$ and $E = 0.15$.

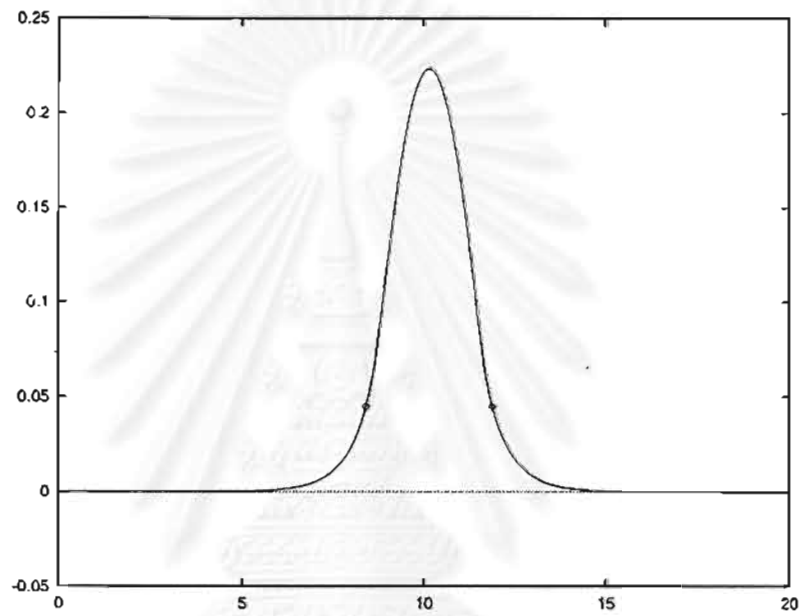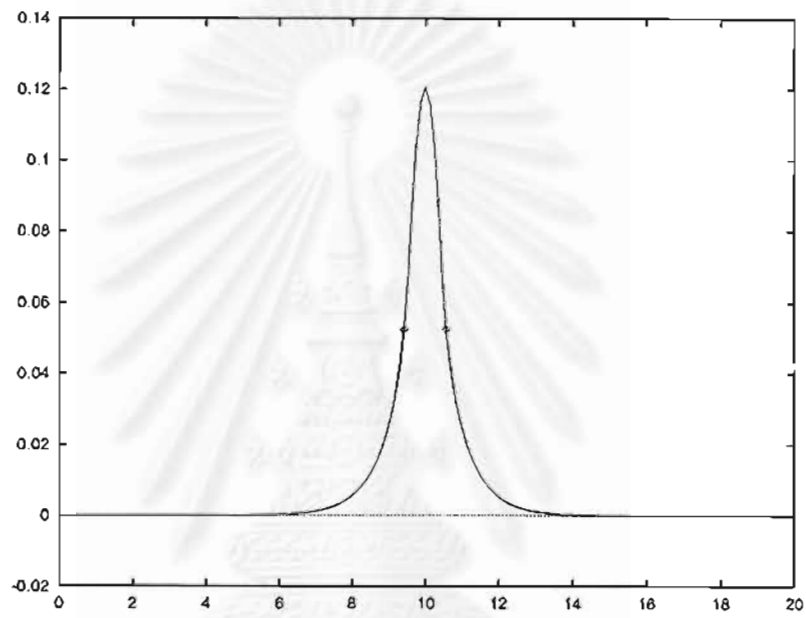Figure 3.3: Typical free-surface profile for $L = 3.0, F^2 = 10.0, \epsilon = 1.0$ and $E = 0.15$.

Figure 3.4: Typical free-surface profile for $L = 1.0, F^2 = 10.0, \epsilon = 1.0$ and $E = 0.15$.

supercritical flow. The numerical accuracy is achieved by increasing M while keeping E fixed and vice versa. We found that the results are independent of M and E, within graphical accuracy, for $M \geq 129$ and $E \leq 0.2$. The solutions converge rapidly after a few iterations. All the results presented here were obtained with $M = 199$ and $E = 0.15$.

Following Vanden-Broeck and Keller (1989), we define the amplitude parameter

$$\alpha = \frac{W}{H} \tag{3.1}$$

Here W is the distance from bottom to maxima or minima of the free surface profile at which the pressure distribution is applied.

When $\epsilon = 0$ (i.e. pressure on the free surface equals to atmosheric pressure p_0), uniform flow, i.e. $\alpha = 1$, is always a solution for $F^2 \geq 1$. From the weakly nonlinear analysis (see Lamb, "Hydrodynamics," 1945), one can also find another solution namely the "solitary wave" solution. This is the solution of the well-known "Korteweg-de Vries" equation that can be expressed by

$$y = (F^2 - 1)\text{sech}^2\left[\left(\frac{3}{4(1 + F^2)}\right)^{\frac{1}{2}}x\right], \quad -\infty < x < \infty$$

It bifurcates from the uniform flow at the critical Froude number $F^2 = 1$. Our numerical results for solitary wave solutions ($\epsilon = 0$) differ by 0.418% of root mean square error from this exact solution. This constitutes a check on our numerical scheme.

It is anticipated that solutions of free-surface flow due to pressure distribution ($\epsilon \neq 0$) is the perturbation of a uniform stream solution, since uniform flow is no longer a solution for any values of F^2 when $\epsilon \neq 0$. Also we expect a perturbed bifurcation of solitary wave solution. To discuss the numerical calculations of supercritical flow regime, we consider 2 cases: $\epsilon > 0$ (positive pressure) and $\epsilon < 0$ (negative pressure).

When $\epsilon > 0$, the solutions are characterized by $\alpha - 1 > 0$. Typical free-surface profiles are shown in Figure 3.3, 3.4 and 3.6. The numerical values of

21

F^2 versus $\alpha - 1$ for a fixed value of $L = 3.0$ and various value of ϵ are presented in Figure 3.5. Figure 3.5 shows that there are two branches of solutions for each ϵ and L. The lower branch (closer to the F^2- axis) can be viewed as perturbation of uniform stream while the upper branch (farther away from the F^2- axis) is the perturbation of solitary wave solution. The nonuniqueness of these solutions can be summarized as follows. There are two critical values, $\tilde{F}_1^2$ and $\tilde{F}_2^2$, of the Froude number F^2 such that, for each ϵ, there are no solutions when $F^2 < \tilde{F}_2^2$, two solutions for $\tilde{F}_2^2 < F^2 < \tilde{F}_1^2$, and one solution for $F^2 > \tilde{F}_1^2$. At the critical value $\tilde{F}_1^2$, a limiting configuration with 120° angle corner at the crest (known as Stokes highest wave) is reached. The other critical value $\tilde{F}_2^2$ signifies the nonlinear effect, i.e., it determines whether there are 2 solutions or no solutions at all.

The upper dashed curve in Figure 3.5 is the limiting configuration for each value of ϵ. We can find such limiting configuration by substituting $y = \alpha - 1$, $q = 0$ and $\tilde{p} = \frac{\epsilon}{e}$ into (2.2). This limiting configuration is characterized by

$$\alpha - 1 = \frac{1}{2}\left(1 - \frac{\epsilon}{e}\right)F^2 \tag{3.2}$$

Relation (3.2) corresponds to the upper dashed curve in Figure 3.5. A typical profile for a value of $F^2 > \tilde{F}_1^2$ is shown in Figure 3.6 and a typical profile for a value of $\tilde{F}_2^2 < F^2 < \tilde{F}_1^2$ are shown in Figures 3.7 and 3.8.

When $\epsilon < 0$, for given ϵ and L, solution exists for all Froude number between $1 \leq F^2 < \infty$ and is unique. This solution can be viewed as perturbation of a uniform stream. Numerical values of F^2 versus $\alpha - 1$ when $L = 3.0$ for various value of ϵ are presented in Figure 3.9. Typical free-surface profiles for $\epsilon = -1.0$ are shown in Figures 3.10 and 3.11.
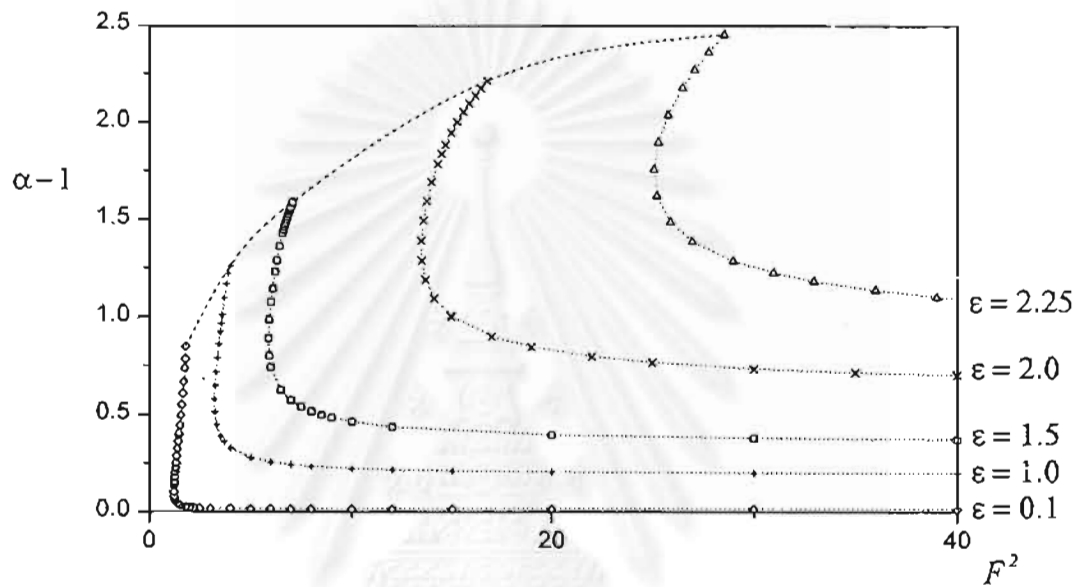
Figure 3.5: Plot of amplitude $\alpha - 1$ versus F^2 for various values of $\epsilon > 0$ when $L = 3.0$. The upper dashed curve represents limiting configurations satisfying equation (3.2).
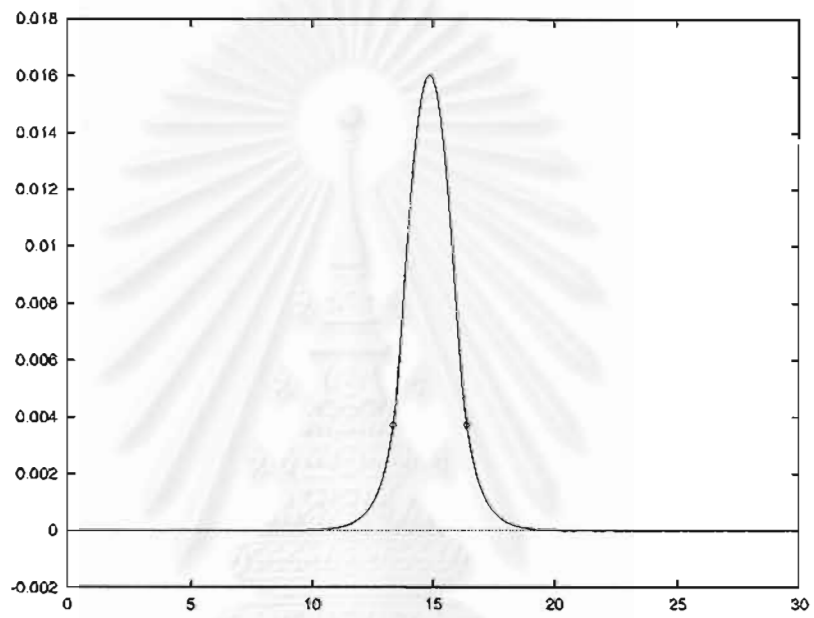
23

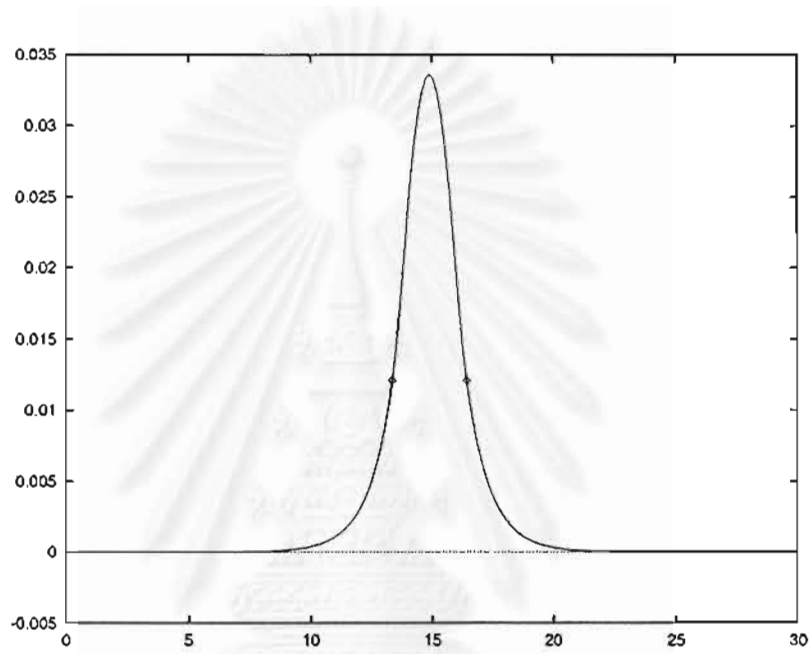Figure 3.6: Typical free-surface profile for $L = 3.0, F^2 = 10.0, \epsilon = 0.1$ and $E = 0.15$.

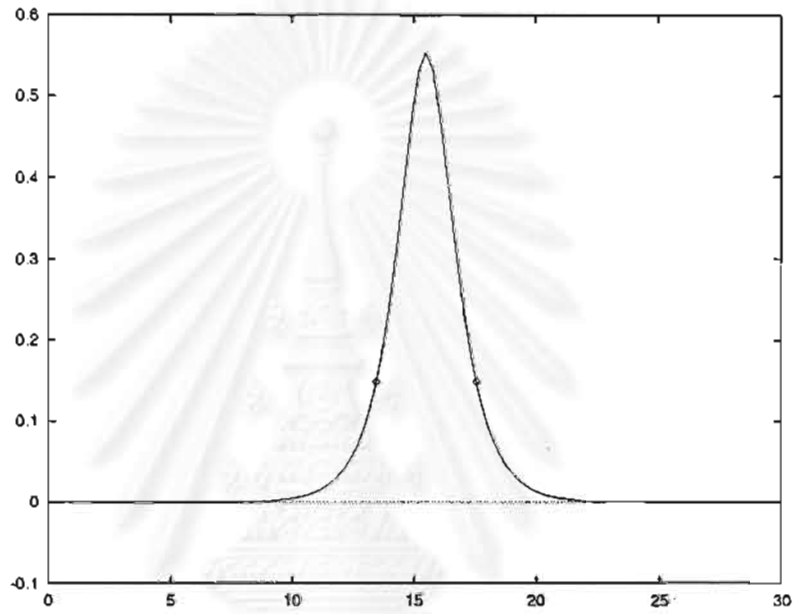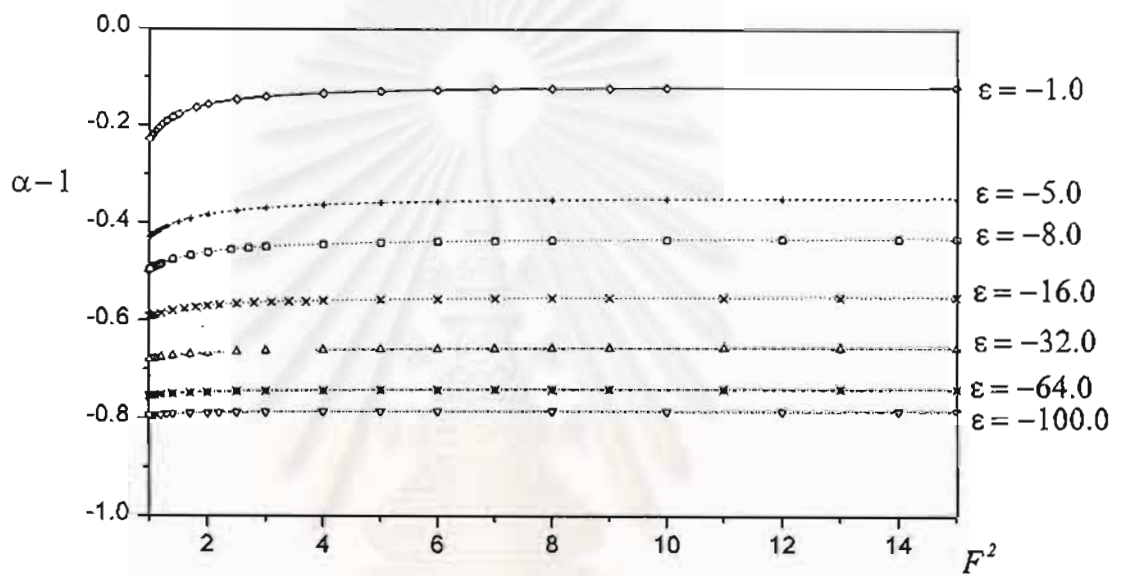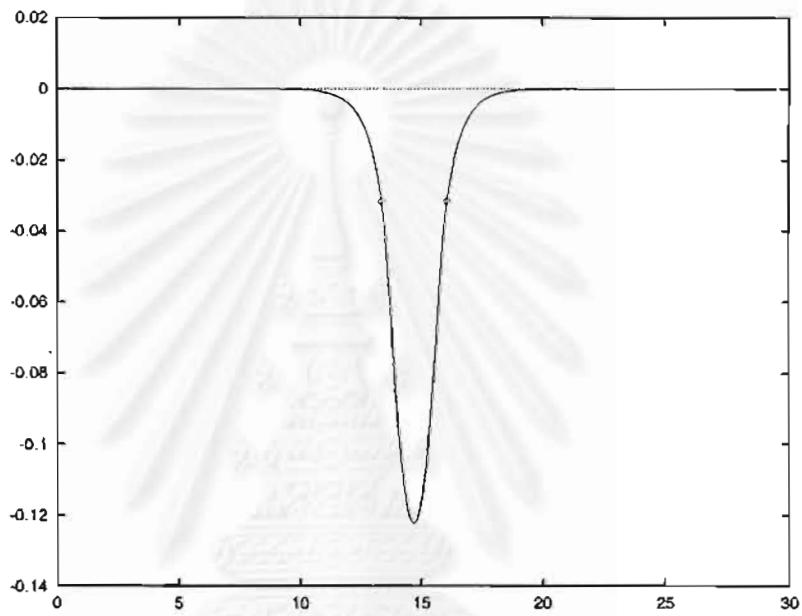Figure 3.7: Typical free-surface profile for $L = 3.0, F^2 = 1.6, \epsilon = 0.1$ and $E = 0.15$.

Figure 3.8: Typical free-surface profile for $L = 3.0, F^2 = 1.6, \epsilon = 0.1$ and $E = 0.15$.

Figure 3.9: Plot of amplitude $\alpha - 1$ versus F^2 for various values of $\epsilon < 0$ when $L = 3.0$.

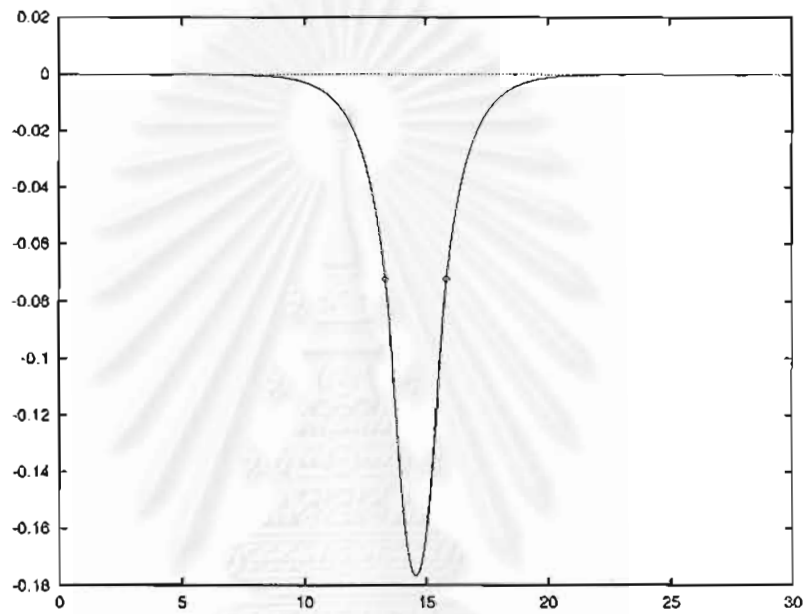Figure 3.10: Typical free-surface profile for $L = 3.0, F^2 = 10.0, \epsilon = -1.0$ and $E = 0.15$.

Figure 3.11: Typical free-surface profile for $L = 3.0, F^2 = 1.5, \epsilon = -1.0$ and $E = 0.15$.

3.2 Subcritical Flow

In this section, numerical solutions in the subcritical flow regime (i.e., $F^2 < 1$) are presented and discussed. We found that, when $F^2 < 1$, the flow is characterized by a train of periodic waves behind the pressure distribution while the upstream free surface satisfies the radiation condition ($v \to 0$ as $x \to -\infty$). Since symmetry of the flow configuration is not expected, the calculations are performed throughout the upper boundary and radiation condition is imposed at the first mesh point $v_1 = 0$ at ϕ_1. Typical profiles for $\epsilon = \pm 0.1$ with $F^2 = 0.25$ and $L = 0.39$ are given in Figures 3.12 and 3.13 respectively. Unlike the case of supercritical flows, the truncation of computational flow domain (M) and the interval or mesh spacing of discretization (E) play significant role when we try to achieve better solution accuracy even to obtain converged solutions. We also find that mesh location at which the pressure is acting does affect the accuracy of the computed solutions while keeping other parameters unchanged. This is discussed in the next paragraph. To check the sensitivities of M and E on the computed solutions, we increase M while keeping E fixed and vice versa until the required accuracy is achieved. This is illustrated in Figures 3.14, 3.15, 3.16 and 3.17. Most of our calculations in this flow regime are performed with $E = 0.065$ and $M = 199$.

It is apparent from Figures 3.18 and 3.19 that accuracy of the solutions is also sensitive to the position of the applied pressure distribution on the free surface. The occurrence of small amplitude periodic disturbance is detected on the upstream free surface when left-end of applied pressure is at $x = 12.50$. This oscillation is nonphysical and computationally contaminated the solutions. This is illustrated in Figure 3.18. As we shift this left-end slightly to $x = 12.30$, the computed free surface profile is significantly improved (see Figure 3.19).
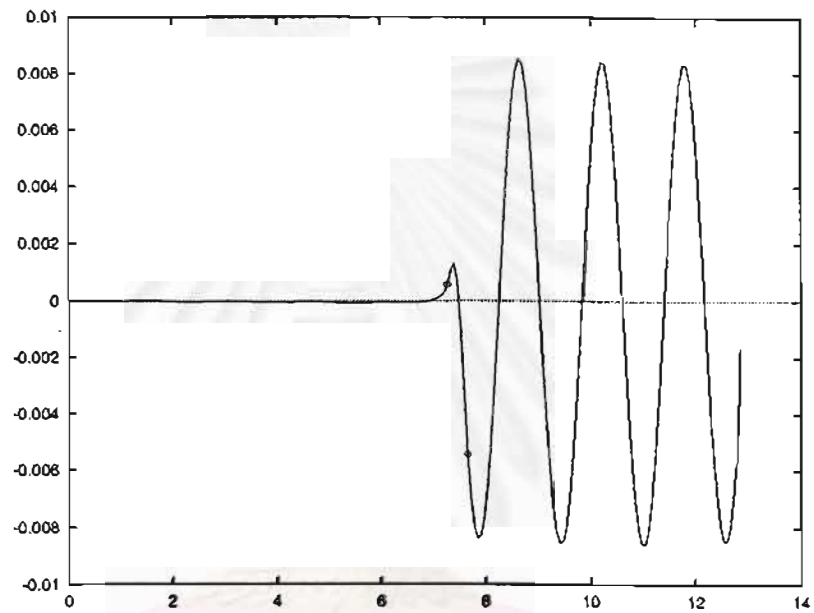
Figure 3.12: Typical free-surface profile for $L = 0.39, F^2 = 0.25$ and $\epsilon = 0.1$.
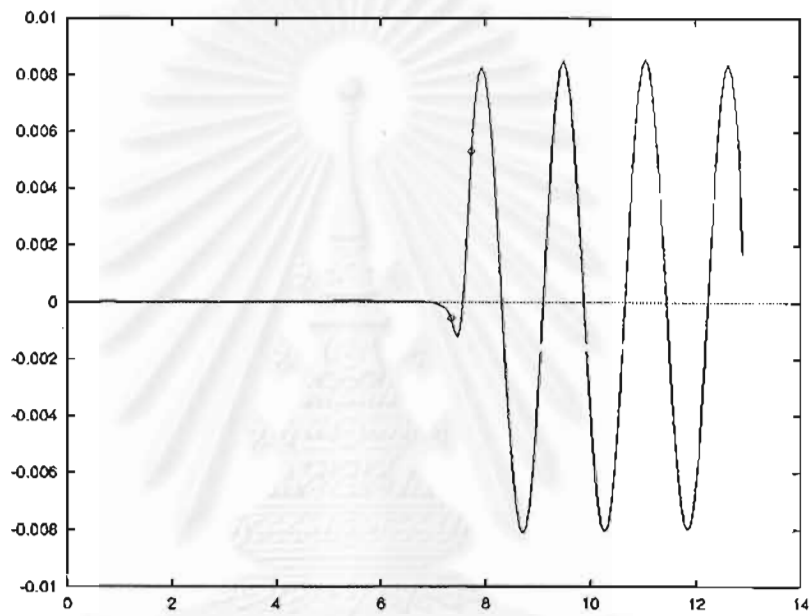
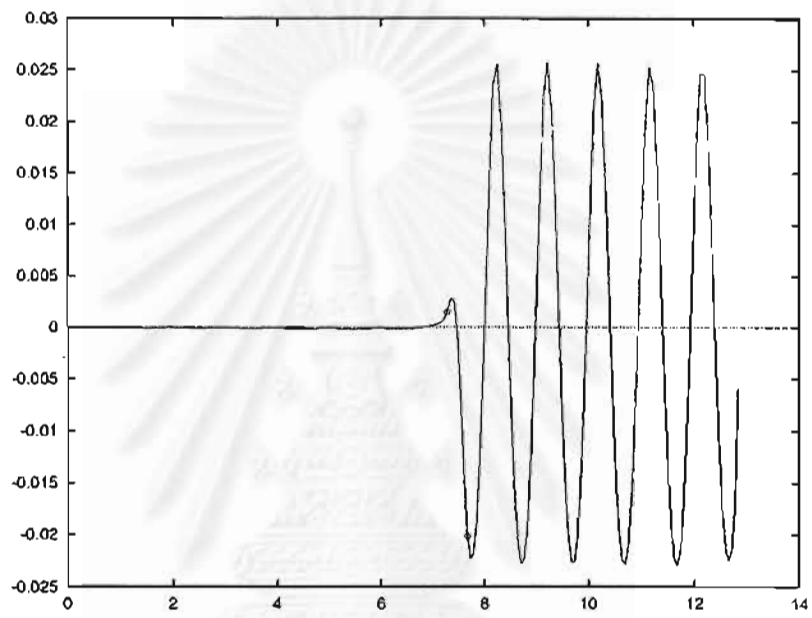Figure 3.13: Typical free-surface profile for $L = 0.39$, $F^2 = 0.25$ and $\epsilon = -0.1$.
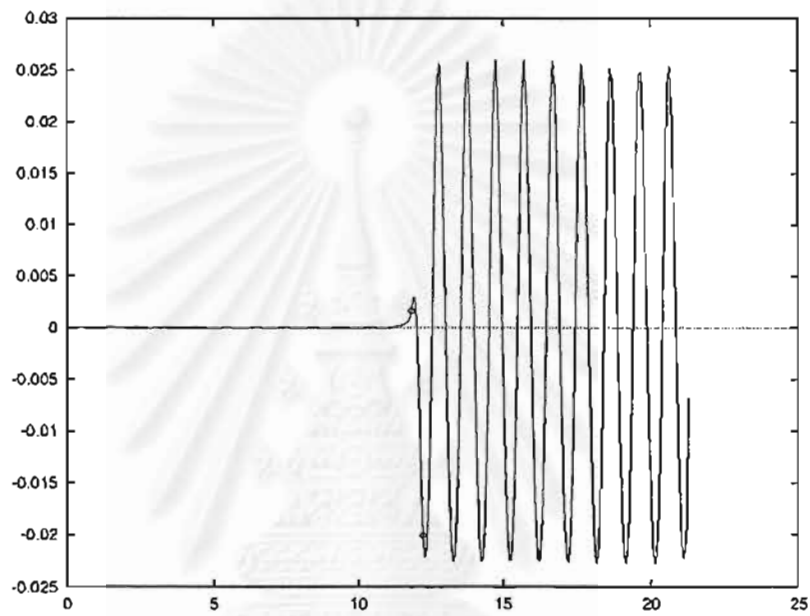
Figure 3.14: Typical free-surface profile for $L = 0.39$, $F^2 = 0.16$, $\epsilon = 0.3$ and $M = 199$.

Figure 3.15: Typical free-surface profile for $L = 0.39, F^2 = 0.16, \epsilon = 0.3$ and $M = 329$.
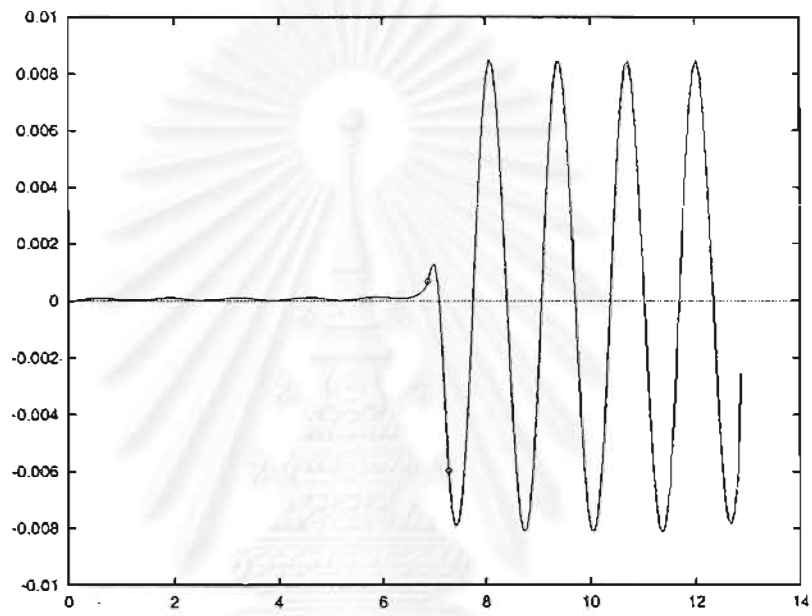
Figure 3.16: Typical free-surface profile for $L = 0.39$, $F^2 = 0.21$, $\epsilon = 0.1$ and $E = 0.065$.
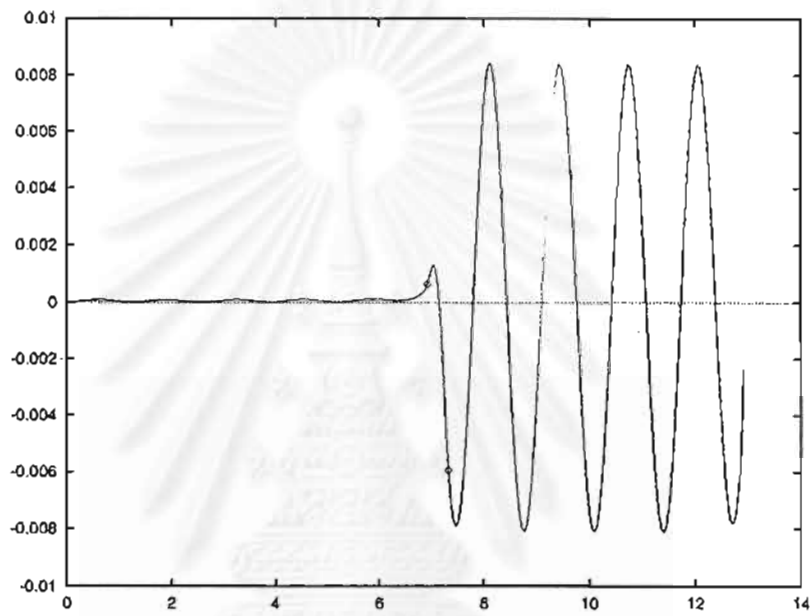
Figure 3.17: Typical free-surface profile for $L = 0.39$, $F^2 = 0.21$, $\epsilon = 0.1$ and $E = 0.04875$.
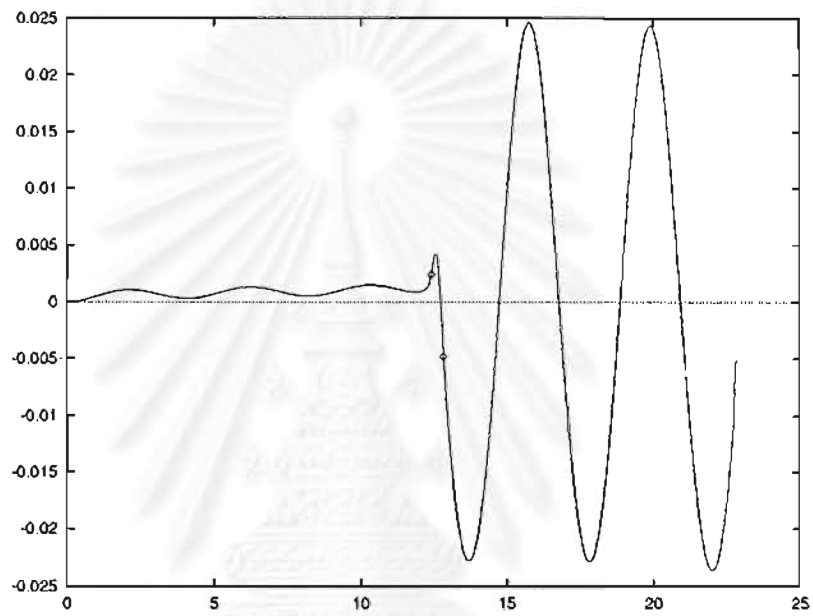
Figure 3.18: Typical free-surface profile for $L = 0.39$, $F^2 = 0.601$ and $\epsilon = 0.1$ (the left-end of applied pressure is at $x = 12.50$).
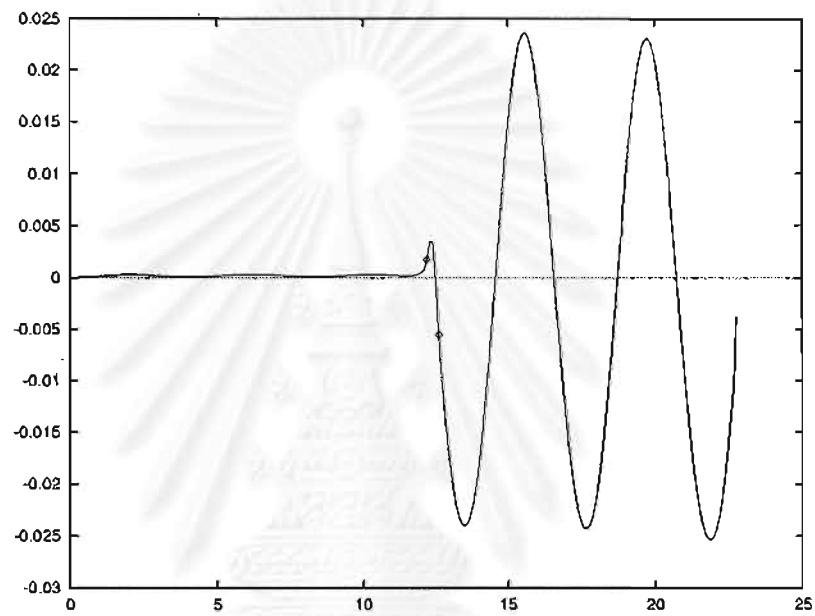
Figure 3.19: Typical free-surface profile for $L = 0.39, F^2 = 0.601$ and $\epsilon = 0.1$ (the left-end of applied pressure is at $x = 12.30$).

As $F^2 \uparrow 1$, the wave amplitude and steepness increase and more mesh points are needed to capture waves behind the pressure distribution. This is computationally expensive and hence the calculations are limited only for $F < 0.8$.

Let us now define the wave amplitude A as the difference between the levels of the successive crest and trough. It can be seen from Figures 3.20 and 3.21 that, for the same value of Froude number, the wave amplitude increases as ϵ gets bigger (i.e. larger magnitude of pressure distribution). We observe from the relationships between wave amplitude A and Froude number F (see Figure 3.22) that there are critical values F_* so that the wave amplitude vanishes. We conjecture that there are finitely many F_* such that $0 < ... < F_{*2} < F_{*1} < 1$. Some of these critical values are given in Table 3.1.

F_{*1}	0.1897
F_{*2}	0.1414
F_{*3}	0.1204
F_{*4}	0.1025

Table 3.1: Critical values F_* of Froude number for $L = 0.39$ and $\epsilon = 0.1$ (see also Figure 3.33).

Numerical calculations show that the subcritical solutions depend on three parameter F, ϵ and L. It is observed that the behavior of solutions is quanlitatively similar for different values of L. Thus it suffices to present results when $L = 0.39$ and $L = 0.65$. The flow reduces to uniform stream as $\epsilon \downarrow 0$.

The wave drag D is calculated by integrating the pressure distribution p over the deformed surface. That is

$$D = \int p n_x ds = \int p \frac{dy}{dx} dx = \int p dy \qquad (3.3)$$

39

Here n_x is the x-component of the outward unit normal vector to the free surface. The wave drag versus the Froude number for various values of $\epsilon > 0$ are shown in Figure 3.23. In addition, the steepness s of the waves, defined as the height between a creast and a trough divided by the wavelength, is presented in Figure 3.24.

When $F > F_{*1}$, the wave amplitude A increases with F^2 whereas the drag D and the steepness s increase to their maximum values and then decrease as $F^2 \uparrow 1$. For each ϵ, when the Froude number lies between the two consecutive critical values $F_{*i}^2 < F^2 < F_{*i-1}^2$ for $i = 2, 3, ...$, the amplitude, drag and steepness increase to their peaks and decrease as the Froude number F^2 decreases between the values F_{*i-1}^2 and F_{*i}^2. Similarly, the results for $L = 0.39$ and $\epsilon < 0$ are presented in Figure 3.25-3.27. We found that the behavior of these numerical values is quanlitatively similar for $\epsilon > 0$. Thus, it is sufficient to present results for the case $\epsilon > 0$.

We further investigate the behavior of solution for $L = 0.65$ and $\epsilon > 0$. The plots of amplitude, wave drag and steepness versus F are presented in Figure 3.28, 3.29 and 3.30 respectively. It is shown that the behavior of solutions for $L = 0.65$ are similar to the solutions for $L = 0.39$.

The comparison of wave amplitude, steepness, drag and Froude number relationships in Figures 3.22, 3.23, 3.24 and 3.28, 3.29, 3.30 shows that the span length of pressure distribution does have the impact on the wave resistance. Particularly, the wave amplitude, steepness and drag increase when the span length L increase. In addition, the critical value F_{*i}^2 for which the drag-free solutions exist are shifted to larger values for bigger value of L (see Table 3.2).

Typical profiles of the drag-free solutions as the Froude number approaches F_{*1}^2 and F_{*2}^2 are shown in Figures 3.31 and 3.32 respectively. Besides the decreasing amplitude of the deformed free surface, we observe that two "humps" occurs as $F^2 \to F_{*2}^2$ while only one "hump" is detected when $F^2 \to F_{*1}^2$. The

40

L	F_{*1}^2
0.39	0.036
0.65	0.065
0.78	0.078

Table 3.2: Critical values of Froude number F_{*1} for various values of L.

numerical results show that as $F^2 \to F_{*n}^2$, there are n "humps" on the free surface of the drag-free solutions. Various values of critical Froude number in the case of $L = 0.39$ and $\epsilon = 0.1$ are shown in Figure 3.33.

It is found that this similar behavior of subcritical solutions exists in the case $\epsilon < 0$ and the other values of L. In order to obtain the waves solutions for the Froude number less than critical value F_{*3}^2 are very difficult. This is because of the decreasing trend of wave length. Thus we are required to use smaller mesh spacing and more mesh points in the computations in order to capture accurate results.
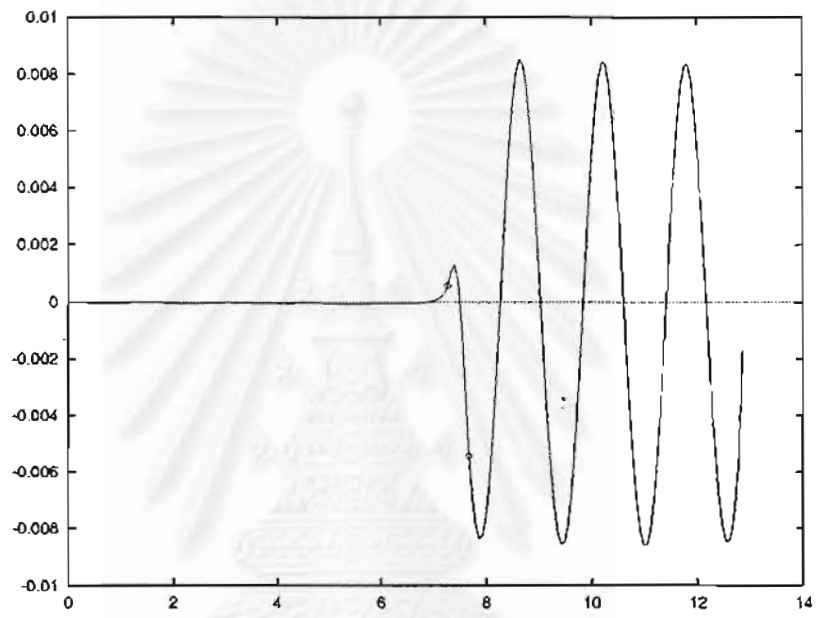
Figure 3.20: Typical free-surface profile for $L = 0.39$, $F^2 = 0.25$ and $\epsilon = 0.1$.
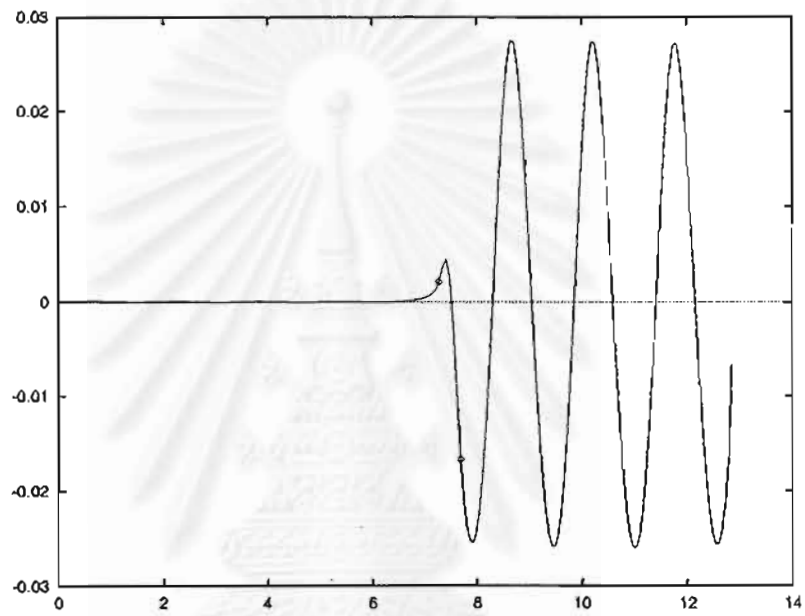
Figure 3.21: Typical free-surface profile for $L = 0.39$, $F^2 = 0.25$ and $\epsilon = 0.3$.
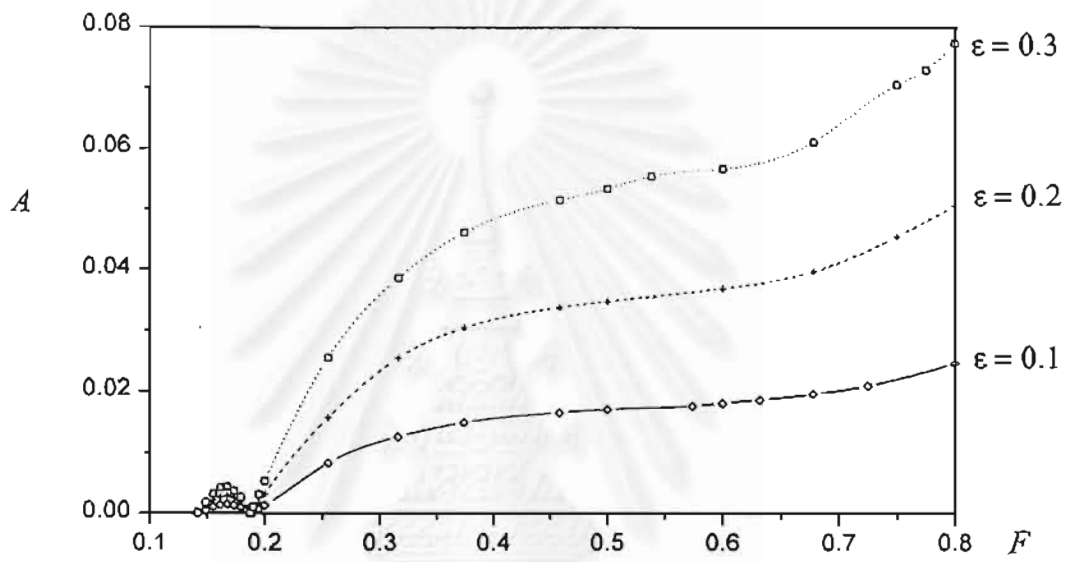
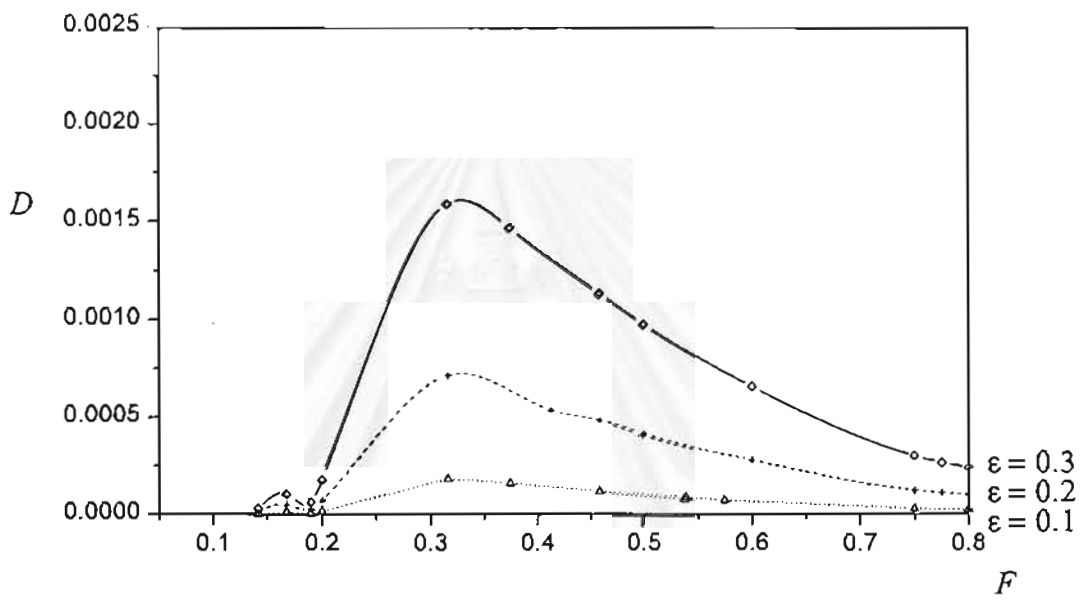Figure 3.22: Plot of amplitude A versus F for $L = 0.39, \epsilon = 0.1, 0.2$ and 0.3.

Figure 3.23: Plot of wave **drag D versus F for $L = 0.39, \epsilon = 0.1, 0.2$ and 0.3.**

Figure 3.24: Plot of steepness s versus F for $L = 0.39, \epsilon = 0.1, 0.2$ and 0.3.

Figure 3.25: Plot of amplitude A versus F for $L = 0.39, \epsilon = -0.1, -0.2$ and -0.3.

Figure 3.26: Plot of wave drag D versus F for $L = 0.39, \epsilon = -0.1, -0.2$ and -0.3.
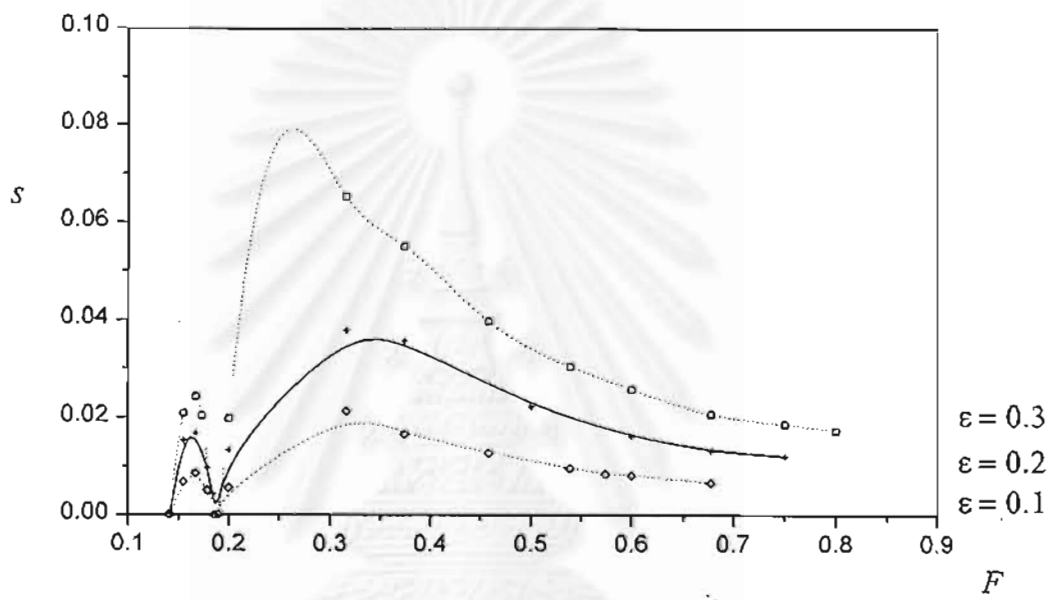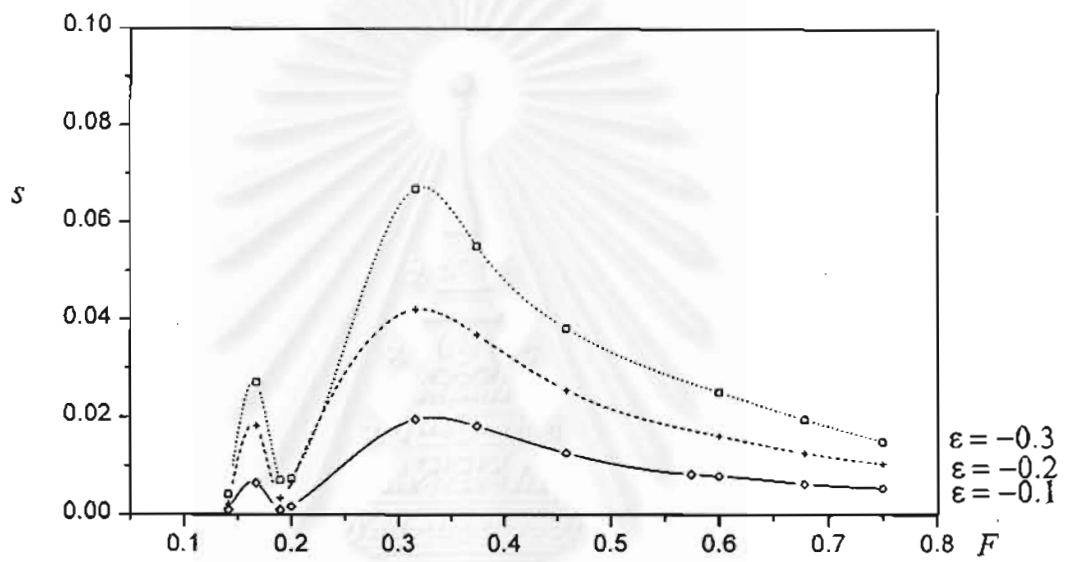
Figure 3.27: Plot of steepness s versus F for $L = 0.39, \epsilon = -0.1, -0.2$ and -0.3.
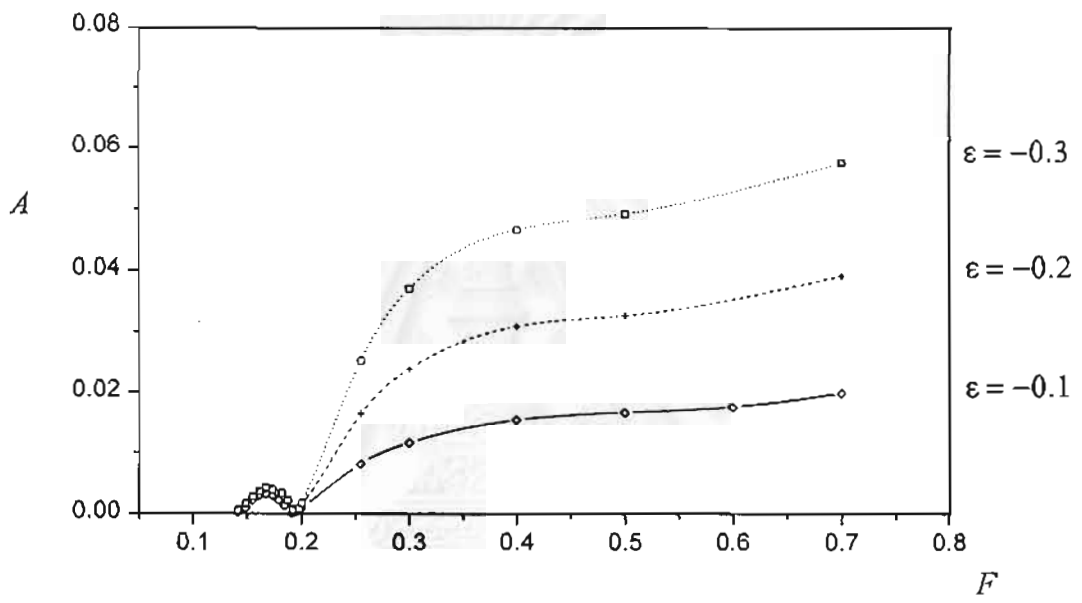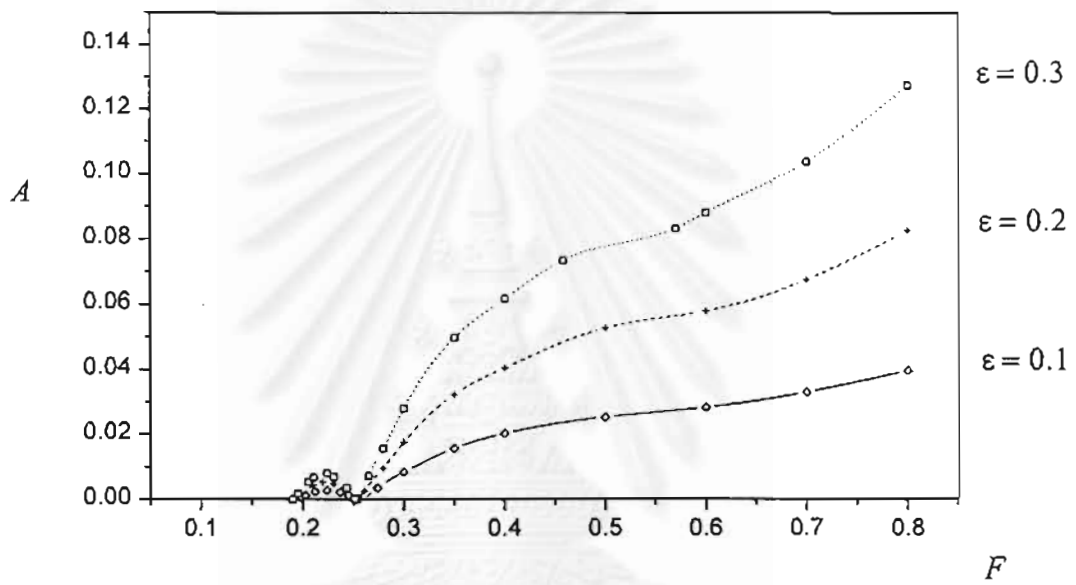
Figure 3.28: Plot of amplitude A versus F for $L = 0.65, \epsilon = 0.1, 0.2$ and 0.3.
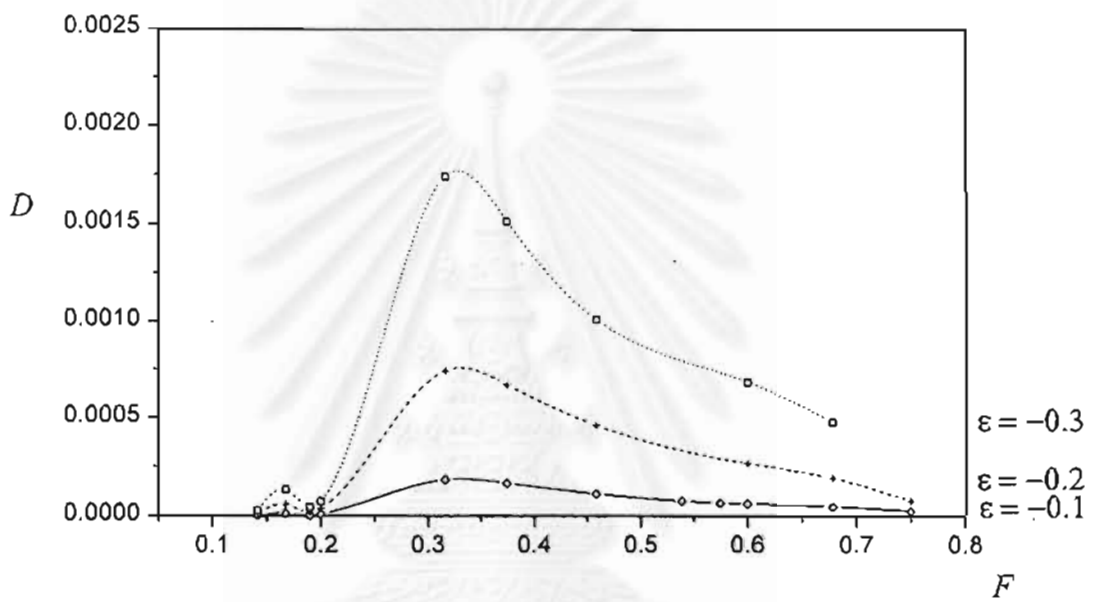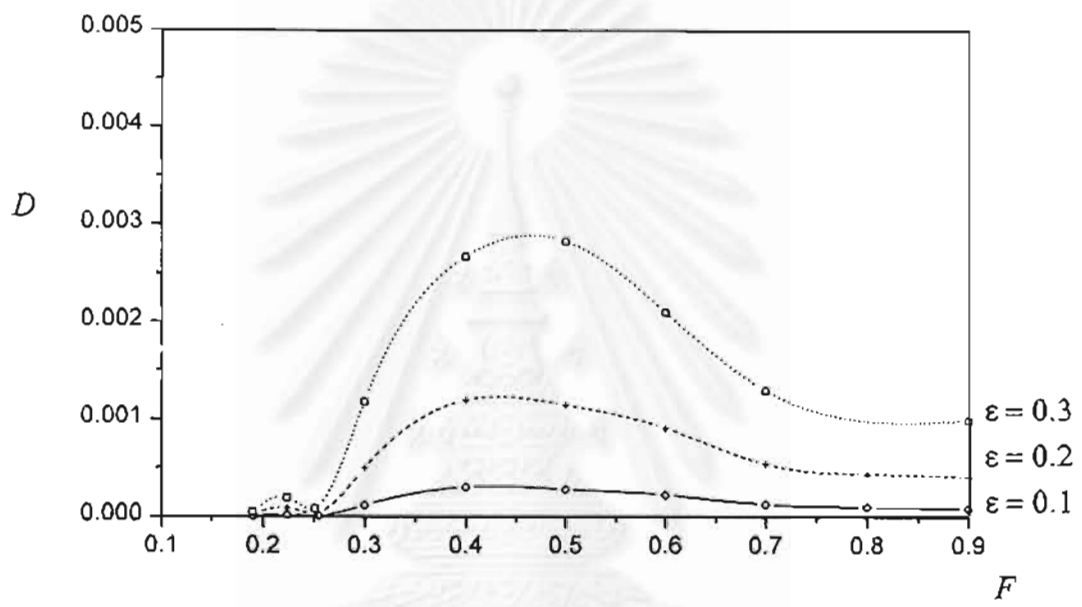
Figure 3.29: Plot of wave drag D versus F for $L = 0.65, \epsilon = 0.1, 0.2$ and 0.3.
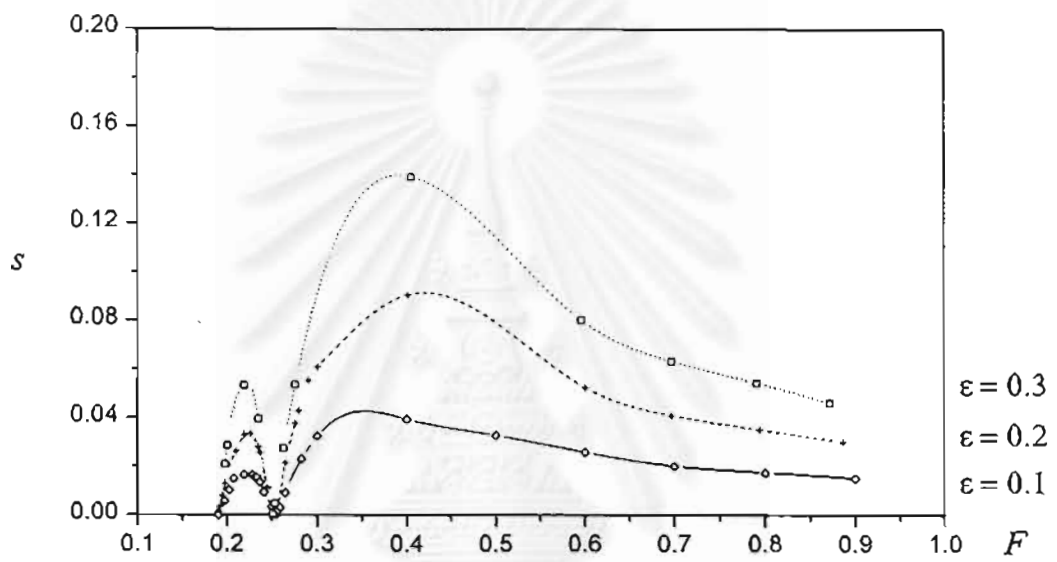
Figure 3.30: Plot of steepness s versus F for $L = 0.65, \epsilon = 0.1, 0.2$ and 0.3.
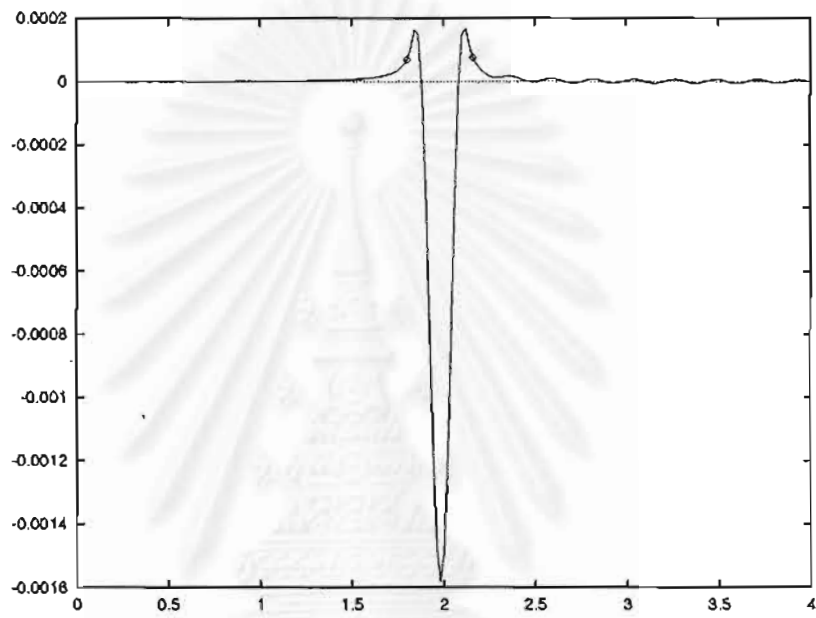
Figure 3.31: Typical free-surface profile of drag-free solution when $L = 0.39$, $F^2 = 0.036$ and $\epsilon = 0.1$.

Figure 3.32: Typical free-surface profile of drag-free solution with two "hump" when $L = 0.39$, $F^2 = 0.020$ and $\epsilon = 0.1$.

Figure 3.33: Plot of amplitude A versus F for $L = 0.39$ and $\epsilon = 0.1$.

3.3 Conclusions

Von Kerczek and Salvesen (1977) solved the nonlinear pressure-distribution problem in water of finite depth by using finite defference scheme for Laplace's equation. Over-relaxation technique together with a network of mesh points all over the fluid d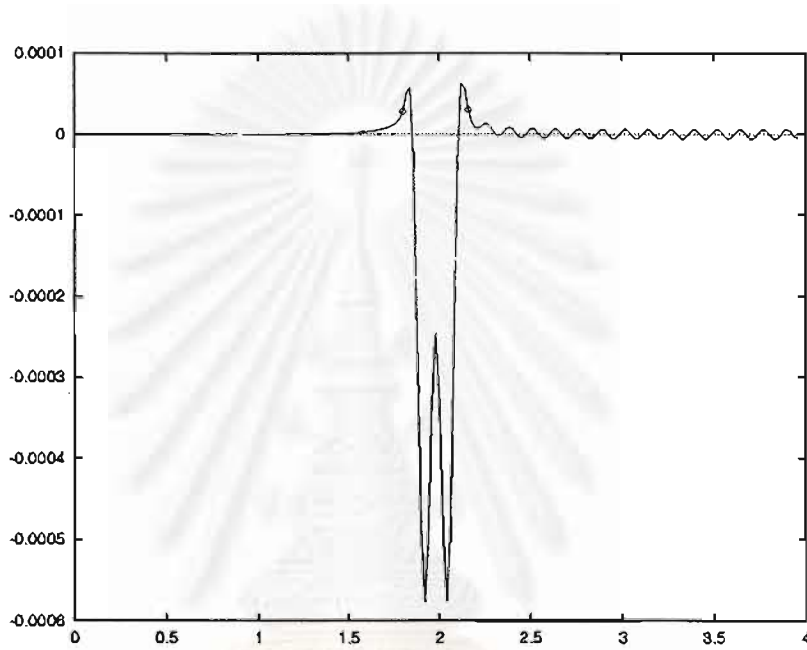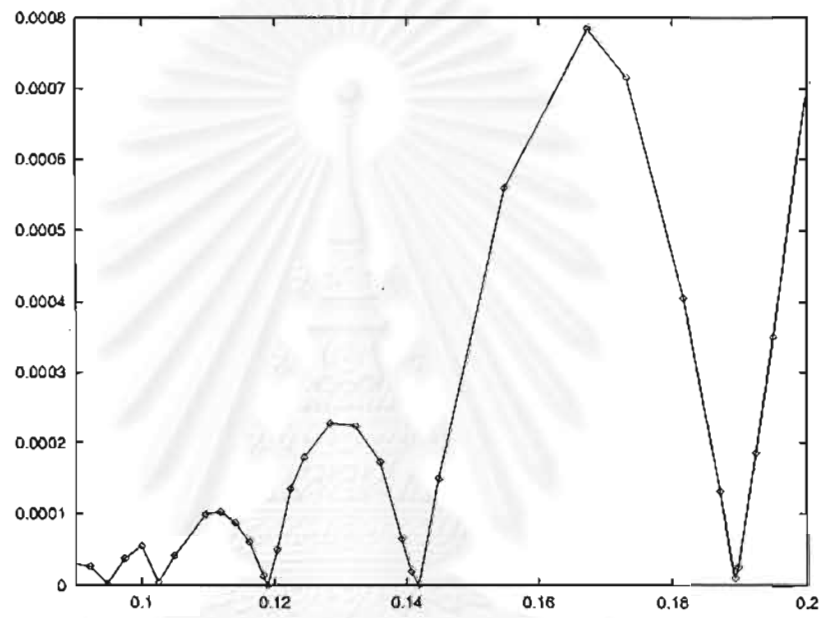omain were employed in the calculations. They found that, for subcritical flow solutions, a train of nonlinear waves was generated behind the applied pressure distribution. Drag-free (symmetric) solutions were found at the critical Froude number $F'_*(0 < F'_* < 1)$. It should be noted here that they defined the Froude number based on the span length of pressure distribution which is different from ours. Solutions at two critical values of Froude number, $0 < F'_{*2} < F'_{*1} < 1$, were presented for various values of pressure coefficient (magnitude of pressure distribution). When $F > F'_{*1}$, the wave resistance increased to their maximum value and the decrease as $F \uparrow 1$. When $F'_{*2} < F < F'_{*1}$, the wave resistance increased to its peak and decreased as the Froude number F approached F'_{*2}. In addition, they found a "hump" on the free surface as $F \to F'_{*1}$ while two "humps" were detected as $F \to F'_{*2}$. Their numerical solutions are qualitatively similar and in good agreement with our results.

Schwartz (1981) used a boundary integral equation technique based on Cauchy's integral formula to solve the steady two-dimensional potential flow past a fixed pressure distribution on the free surface. Fluid was assumed to be of infinite depth. Nonlinear subcritical solutions with narrow crests and broad troughs on the downstream waves were presented. The wave resistance coefficient for various values of Froude number was calculated and compared to the linear theory. He found that, for subcritical flow solutions in deep water, the wave resistance was identically zero at certain values of the span length of pressure distribution ($L = \frac{2}{F^2} = 4\pi, 8\pi, ...$), i.e. when the ship length was an integer multiple of a free wave length. This was similar to the linear theory

except a phase shift. Thus, there were finitely many Froude numbers at which the flows would be drag-free. In our computations, the solutions show similar behaviors to those of infinite depth when $\frac{wavelength}{depth} \ll \frac{1}{2}$.

Inverse problem to flows due to applied pressure distribution is the problem of flows over a semi-circular obstruction considered by Forbes and Schwartz (1982). They constructed an integral equation involving flow variables at the free surface so that the bottom boundary condition is automatically satisfied. The exact nonlinear equations were solved numerically at the free surface by a process of Newtonian iterations. In the subcritical case, they showed that, there exist flows with essentially wave-free upstream profile and a train of nonlinear Stokes waves on downstream profile. When the circle radius increased or $F \uparrow 1$, the wave amplitude and the wave drag also increased. This behavior is observed in our numerical results for the case of larger values of ϵ. In the supercritical case, they found symmetric solutions with respect to the axis of symmetry of the semicircle. For a large value of Froude number, the nonlinear free surface profile is ultimately limited by the formation of a sharp crest with sides that enclose an angle of 120°. We can observe such behavior in our supercritical solutions. This can be seen on the upper dash curve in Figure 3.5 which is our limiting configuration.

Asavanant and Vanden-Broeck (1994) studied the steady two-dimensional flows past a parabolic obstacle lying on the free surface in water of finite depth. The object was described by $y = \frac{1}{2}\epsilon(x - x_0)^2 + y_0$. Here (x_0, y_0) represented the vertex of the object and ϵ was the object geometry (object was concave if $\epsilon > 0$, convex if $\epsilon < 0$ and flat if $\epsilon = 0$). The problem was solved numerically by using boundary integral equation technique based on the Cauchy's integral formula. An integral equation was solved together with the dynamic free-surface condition. They satisfied the bottom boundary condition by employing the reflection principle. For supercritical flows past a concave

57

object ($F > 1, \epsilon > 0$), they found two different types of solutions. Solutions of first type were characterized by $\alpha - 1 < 0$, i.e. the vertex of the obstacle was below the level of the free surface at infinity. These solutions modeled a ship moving at a constant velocity in a channel. For a given $\epsilon > 0$, solution existed for all Froude number between $1 \leq F^2 < \infty$ and was unique. In addition, $\alpha - 1$ increased as ϵ increased. Clearly, the first type of their solutions are similar to ours when $F > 1$ and $\epsilon < 0$ (see also Figure 3.9). Solutions of the second type were characterized by $\alpha - 1 > 0$, i.e. the vertex of the obstacle was above the level of the free surface at infinity. These solutions modeled a surfboard riding on a wave. For supercritical flows past a convex object ($F > 1, \epsilon < 0$), they found one type of solutions that were characterized by $\alpha - 1 > 0$. Their numerical results showed that there were nonuniqueness of solutions. In particular, one solution was a perturbation of uniform stream while the other solution was a perturbation of solitary wave solution. Our numerical results for supercritical flows appear to be similar to their in the case of $F > 1$ and $\epsilon > 0$ (see also Figure 3.5). Their subcritical solutions showed that a train of (linear) sine waves was generated for larger values of F. These waves developed narrow crests and broad troughs as F decreased. Finally, they conjectured that these waves would approach their limiting configurations characterized by a 120° angle corner at the crests. This is in contrast with our results. In particular, our subcritical flow solution never posses the Stokes' limiting configuration but they will reach drag-free solutions at critical Froude numbers.

Chapter 4
Flows with Gravity-Capillary Waves

4.1 Formulation

Let us consider the steady two-dimensional irrotational flow of an incompressible inviscid fluid past the applied pressure distribution. Fluid domain is bounded above by the free surface and below by the rigid bottom. In this chapter, we include the effects of both gravity g and surface tension T in the dynamic boundary condition on the free surface. It has been known for a long time that the effect of gravity-capillarity results in very complex phenomenon. At this stage of study, we shall restrict ourselves in the case of subcritical symmetric flows due to pressure distribution. Such gravity-capillary waves will be calculated numerically and discussed in section 4.2.

Bernoulli equation on the free surface yields, in dimensional form,

$$\frac{1}{2}q^2 + gy + \frac{p}{\rho} - \frac{T}{\rho}K = \text{constant on the free-surface} \qquad (4.1)$$

where T is the surface tension and K is the curvature of the free surface. We define the curvature K by

$$K = \frac{\eta''(x)}{(1 + \eta'(x))^{\frac{3}{2}}} \; ,$$

where $\eta(x)$ is the vertical displacment of the free surface measured from the undisturbed water level. We determine the constant on the free surface (4.1) by imposing uniform flow condition at $x = -\infty$. This gives,

$$\frac{1}{2}q^2 + gy + \frac{p}{\rho} - \frac{T}{\rho}K = \frac{1}{2}U^2 + gH + \frac{p_0}{\rho} \qquad (4.2)$$

Refering back in chapter 2, we normalize the problem by choosing H as the length scale and U as the velocity scale. Bernoulli equation (4.2), in dimensionless form, appears to be similar to equation (2.2) with additional surface tension term. That is

$$F^2 q^2 + 2y + F^2 \tilde{p} - 2\tau^* K = 2 + F^2 \qquad (4.3)$$

where $\tilde{p} = \frac{p - p_0}{\frac{1}{2}\rho U^2}$ and $\tau^* = \frac{T}{\rho g H^2}$. The dimensionless parameter τ^* is the well known "Bond" number. From the assumption of incompressibility and irrotationality, we shall introduce the complex potential $f = \phi + i\psi$ and the complex velocity $w = u - iv$. Without loss of generality we choose $\phi = 0$ at C and $\psi = 0$ on the free surface AB. By the choice of our dimensionless variable $\psi = -1$ on the bottom (see Figure 4.2). The kinematic condition on the bottom is

$$v(\phi, \psi) = 0 \quad \text{on} \quad \psi = -1 \qquad (4.4)$$

We now reformulate the problem as an integral equation. First we define the function $\tau(\alpha, \beta) - i\theta(\alpha, \beta)$ by

$$w = e^{\tau - i\theta}.$$

We map the flow domain onto the lower half of the ζ- plane by the transformation $\zeta = \alpha + i\beta = e^{\pi f}$. In particular, we have the relations $\alpha = e^{\pi\phi}cos(\pi\psi)$ and $\beta = e^{\pi\phi}sin(\pi\psi)$. The flow in the ζ - plane is shown in Figure 4.3. We choose a contour consisting of a real axis and a half-circle of arbitrary large radius in the lower half plane. Applying the Cauchy integral formula to the function $\tau - i\theta$ in the complex ζ- plane. We have

$$\tau - i\theta = -\frac{1}{2\pi i} \oint \frac{\tau(\zeta') - i\theta(\zeta')}{\zeta' - \zeta} \, d\zeta'$$

Line integral on the path of half-circle vanishes as we let the radius of the half circle goes to infinity. Letting ζ approaches the boundary $\beta = 0$, we obtain
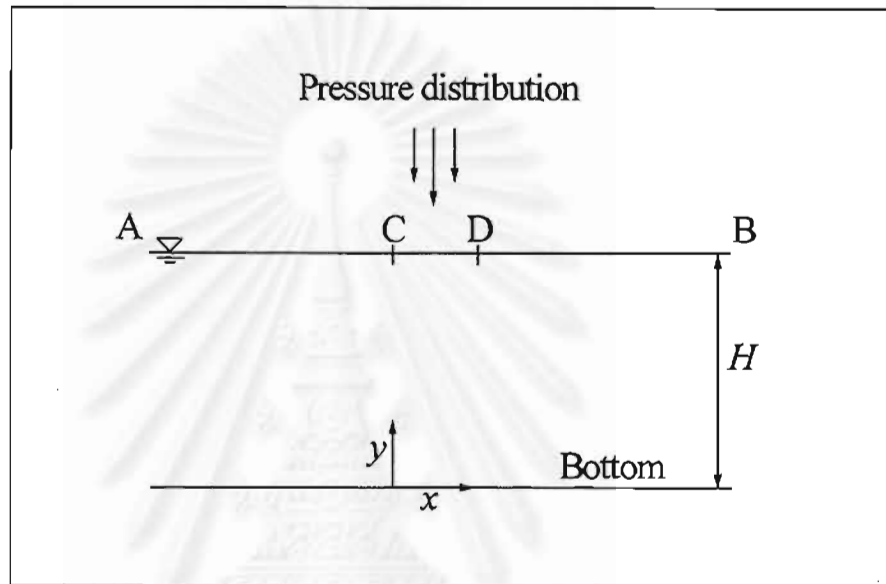
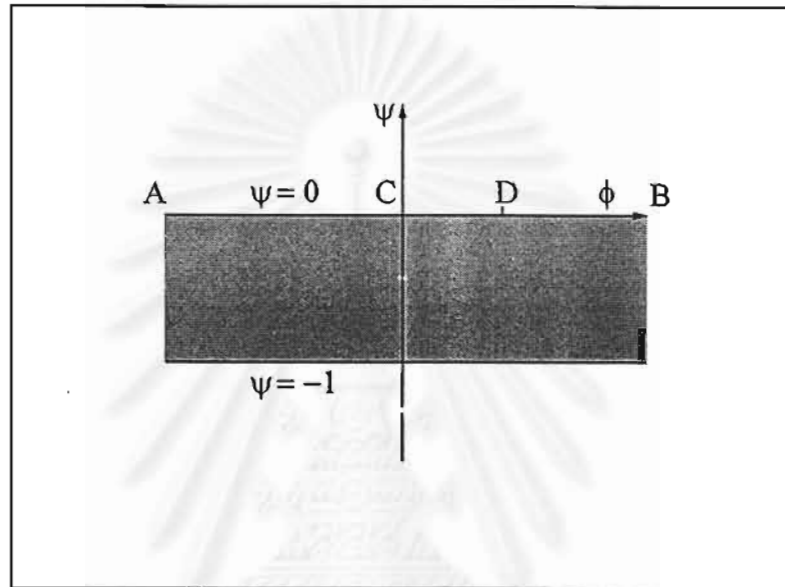Figure 4.1: Sketch of flow domain under the applied pressure distribution between C and D.

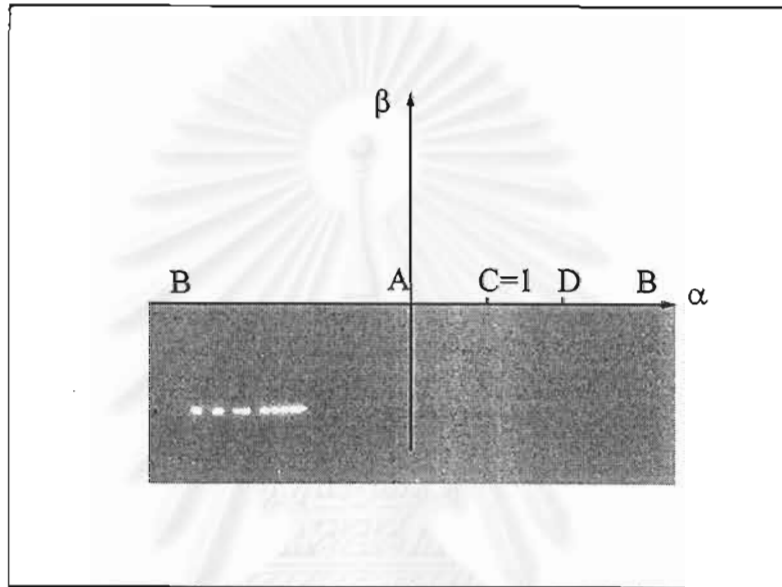Figure 4.2: The complex f- plane by the transformation $f = \phi + i\psi$.

Figure 4.3: The complex ζ- plane by the transformation $\zeta = \alpha + i\beta = e^{\pi f}$.

$$\tau - i\theta = -\frac{1}{\pi i} \int\limits_{-\infty}^{\infty} \frac{\tau(\alpha') - i\theta(\alpha')}{\alpha' - \alpha} \, d\alpha'$$

After taking real part we obtain

$$\tau(\alpha) = \frac{1}{\pi} \int\limits_{-\infty}^{\infty} \frac{\theta(\alpha')}{\alpha' - \alpha} \, d\alpha' \tag{4.5}$$

Detail of the calculation is closely related to the one described in chapter 2. The kinematic condition (4.4) imply that

$$\theta(\alpha) = 0 \quad \text{for} \quad \alpha < 0 \tag{4.6}$$

Substituting (4.6) into (4.5), we will have

$$\tau(\alpha) = \frac{1}{\pi} \int\limits_{0}^{\infty} \frac{\theta(\alpha')}{\alpha' - \alpha} \, d\alpha' \tag{4.7}$$

We obtain another relation between τ and θ on the free surface by using $w = u - iv = e^{\tau - i\theta}$. That is $u^2 + v^2 = e^{2\tau}$. Equation (4.3) then becomes

$$F^2 e^{2\tau} + 2y + F^2 \tilde{p} - 2\tau^* e^\tau \frac{\partial \theta}{\partial \phi} = 2 + F^2 \tag{4.8}$$

Finally, the free surface profile is determined by integrating numerically the identity

$$\frac{dx}{d\phi} + i\frac{dy}{d\phi} = w^{-1} = \frac{cos(\theta) + i sin(\theta)}{e^\tau} \ .$$

That is

$$\frac{dy}{d\phi} = \frac{sin(\theta)}{e^\tau} \ , \tag{4.9}$$

or

$$\frac{dy}{d\alpha} = \frac{e^{-\tau} sin(\theta)}{\pi\alpha} \ . \tag{4.10}$$

Integrating (4.10) yields,

$$y(\alpha) - y(0) = \frac{1}{\pi} \int\limits_{0}^{\alpha} \frac{e^{-\tau} sin(\theta)}{\alpha} \, d\alpha \ , \ 0 < \alpha < \infty.$$

Since $y \to 1$ as $\alpha \to 0$, we have

$$y(\alpha) = 1 + \frac{1}{\pi} \int_0^\alpha \frac{e^{-\tau(\alpha_0)} sin\theta(\alpha_0)}{\alpha_0} \, d\alpha_0 \quad , \quad 0 < \alpha_0 < \alpha, \quad \text{as } \alpha \to \infty \qquad (4.11)$$

Equations (4.7), (4.8) and (4.11) define a nonlinear integral equation for the unknown function $\theta(\alpha)$ on the free surface. This completes the formulation of our problem.

4.2 Numerical Procedure

We solve the system of integral equations (4.7), (4.8) and (4.11) numerically by placing equally spaced points ϕ_i on $\psi = 0$. The transformation from f-plane to ζ- plane gives

$$\alpha = e^{\pi\phi} \tag{4.12}$$

We write $\tau'(\phi) = \tau(e^{\pi\phi})$, $\theta'(\phi) = \theta(e^{\pi\phi})$ and $y'(\phi) = y(e^{\pi\phi})$ for brevity. Equation (4.7) then becomes,

$$\tau'(\phi) = \int\limits_{-\infty}^{\infty} \frac{\theta'(\phi_0)e^{\pi\phi_0}}{e^{\pi\phi_0} - e^{\pi\phi}}\, d\phi_0 \tag{4.13}$$

Similarly we rewrite (4.8) and (4.11) as

$$F^2 e^{2\tau'(\phi)} + 2y'(\phi) + F^2\bar{p} - 2\tau^* e^{\tau'(\phi)}\frac{\partial\theta'}{\partial\phi} = 2 + F^2 \,, \tag{4.14}$$

$$y'(\phi) = 1 + \int\limits_{-\infty}^{\phi} e^{-\tau'(\phi_0)} sin\theta'(\phi_0)\, d\phi_0. \tag{4.15}$$

Since we are interested in symmetric subcritical solutions, following conditions must be imposed

$$\theta(-\phi) = -\theta(\phi)\,, \text{ and } \theta(\phi = 0) = 0.$$

Using the above condition, the integral equation (4.13) can be rewritten as

$$\tau'(\phi) = \int\limits_{0}^{\infty} \frac{\theta'(\phi_0)e^{\pi\phi_0}}{e^{\pi\phi_0} - e^{\pi\phi}}\, d\phi_0 - \int\limits_{0}^{\infty} \frac{\theta'(\phi_0)e^{-\pi\phi_0}}{e^{-\pi\phi_0} - e^{\pi\phi}}\, d\phi_0. \tag{4.16}$$

Next we introduce the equally spaced mesh points

$$\phi_i = (i-1)E \,, \ i = 1, 2, ..., M$$

where E is the discretization interval. We evaluate the values $\tau_{i+\frac{1}{2}}$ of $\tau'(\phi)$ in equation (4.16) at the midpoints

$$\phi_{i+\frac{1}{2}} = \frac{\phi_i + \phi_{i+1}}{2} \,, \ i = 1, 2, ..., M-1$$

66

by using trapezoidal rule with the summation over the points ϕ_i. The symmetry of the quadrature and of the distribution of mesh points enable us to evaluate the integral which is of Cauchy principal value as if it were ordinary integrals (see Appendix). Next we evaluate $y_i = y'(\phi_i)$ by applying the trapezoidal rule to (4.15). That is,

$$y_M = 1.0 \ ,$$

and $\qquad y_{i-1} = y_i - e^{-\tau_{i-\frac{1}{2}}} \sin(\theta_{i-\frac{1}{2}})E \ , \ i = M - 1, ..., 1.$

We use these values to evaluate $y'(\phi)$ at the midpoints by using four-points interpolation formula. We now satisfy the free surface condition (4.14) by substituting these values of $\tau'(\phi)$ and $y'(\phi)$ at the midpoints. This yields $M-1$ nonlinear algebraic equations for the M unknowns $\theta_i, i = 1, ..., M$. Finally, the last equation is obtained by imposing the radiation condition defined as

$$\theta_{i-\frac{1}{2}} = 0 \ \text{at} \ \ i = M - 1.$$

This system of M nonlinear algebraic equations with M unknowns is solved by Newton's Method.

4.3 Numerical Results and Discussions

We use the numerical scheme described in the previous section to compute the gravity-capillary wave solutions for various values of τ^* (Bond number). Most of the calculations are performed with $E = 0.05, M = 199$ and $L = 3.0$. The numerical results show that, for a fixed value of $\tau^* = 0.3$ and $\epsilon = 5.0$, there are two families of solutions at the same Froude number (see Figure 4.7). One family is a purturbed solution of uniform stream (see Figure 4.4) whereas the other is a perturbed solution of solitary wave (see Figure 4.5). The upper curve in Figure 4.7 is a purterbed solution of uniform stream while the lower curve is a purturbed solution of solitary wave. The solid line in Figure 4.7 represent gravity-capillary wave solutions. Solution on the lower curve close to the solid line (perturbation of solitary wave) exhibit sharp and narrow trough at the symmetry line as Froude number decreases. Finally, as the Froude number decreases to its critical value F_{c1}, the limiting configuration is reached in the form of trapped bubble. Figure 4.6 illustrates this trapped bubble configuration. As depicted in Figure 4.6, this critical Froude number appears to be insensitive to the pressure distribution (i.e. same critical Froude number as for $\epsilon = 0.0$ and $\epsilon = 5.0$). Solutions representing the perturbation of uniform stream (upper curve closer to the F- axis) exist for $0 < F < F_{c2}$. As $F \downarrow 0$, the flow configuration approaches a uniform stream. In summry, there are no solution when $F_{c2} < F < 0$, one solution when $F < F_{c1}$, and two solutions when $F_{c1} < F < F_{c2}$.

The numerical results for $\tau^* = 0.5$, $\epsilon = 0.0$ and $\epsilon = 5.0$ are presented in Figure 4.8. As we can see, the solutions in this case are qualitatively similar to the case of $\tau^* = 0.3$ (i.e. there are two families of solution). However, the bahavior of solution at the critical value F_{c1} does not approach a limiting configuration with trapped bubble. Instead, the free surface profile is close to the flow configuration due to sink as shown in Figure 4.9. We observe that

68

for $\tau^* \geq 0.5$, no limiting configuration in the form of trapped bubble can be found.

When $\tau^* = 0.25$, the typical free surface profile for $\epsilon = 0.01$ is presented in Figure 4.10. We found that the free surface profile develops a large number of inflexion points as τ^* decrease. The computation is very difficult to get solutions when τ^* is very small. This is because smaller discretization interval is needed and more mesh points are required to achieve better numerical accuracy.

Typical free-surface profiles for two different Froude number when $\epsilon = -0.01$ and $\tau^* = 0.25$ are illustrated in Figures 4.11 and 4.12. It is worthwhile noting that, when $\tau^* = 0.25$ and $F = 0.5$, the computed solutions are qualitatively similar to the case of supercritical flows with no surface tension, whereas when $\tau^* = 0.25$ and $F = 0.9592$, our solutions develop more inflexion points on the free surface.

The case of two-dimensional gravity-capillary solitary waves in water of finite depth without applied pressure distribution was considered by Hunter and Vanden-Broeck (1983). Fully nonlinear problem was formulated as a system of integro-differential equations and solved numerically. Their calculations showed that, for the case of gravity-capillary solitary waves, the critical configuration in the form of trapped bubble at the trough can be obtained when $\tau^* < \frac{1}{2}$. They concluded that, the free surface profiles develop a large number of inflexion points when τ^* is smaller than $\frac{1}{3}$. On the other hand, wave profile becomes steeper and distance between the trough and the bottom decreases as $\tau^* > \frac{1}{2}$. Such wave profile shall approach a static limiting configuration (distance between the trough and the bottom approaches zero) in which gravity is balanced by surface tension. In general, Hunter and Vanden-Broeck's results described here are found to be similar to ours. However, we have shown here that more solutions can be obtained when there is an applied pressure

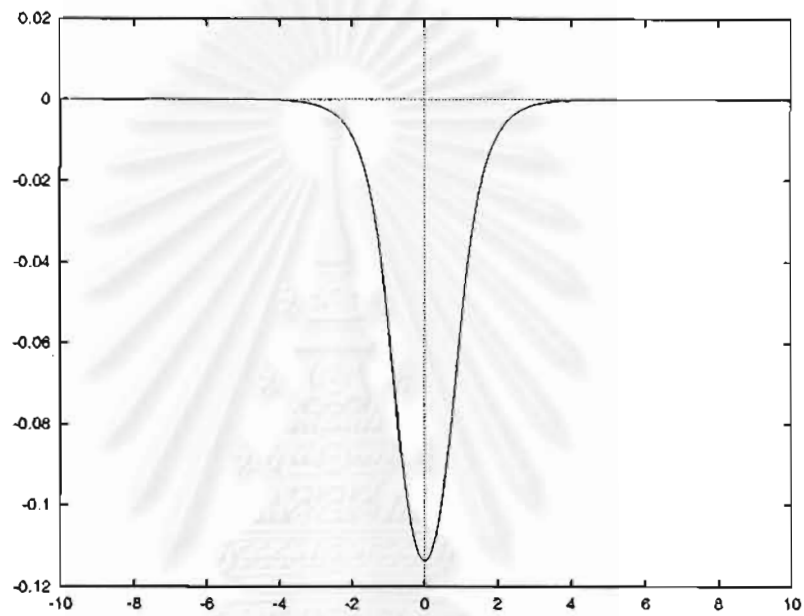distribution in comparison with Hunter and Vanden-Broeck's results.

Figure 4.4: Typical free-surface profile for $F = 0.3742$, $\epsilon = 5.0$ and $\tau^* = 0.3$. This solution is perturbed by uniform flow solution.
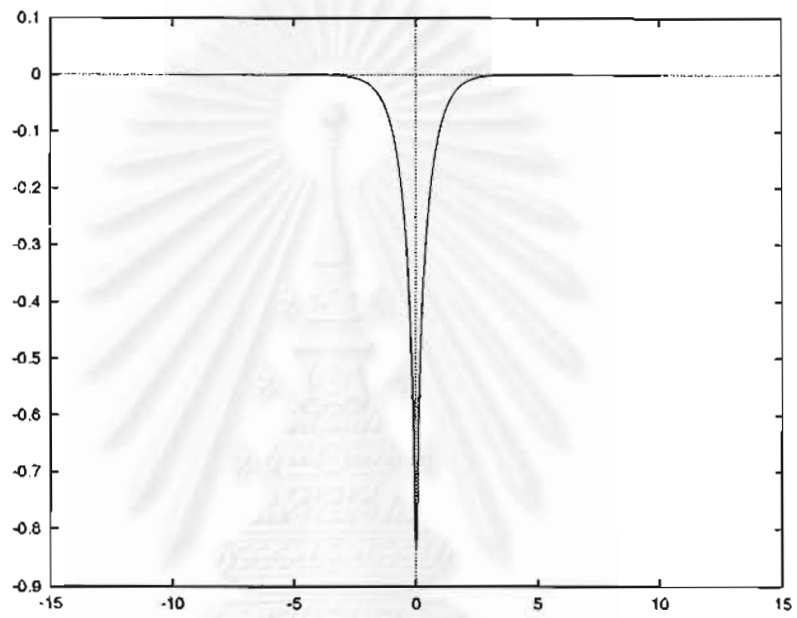
71

Figure 4.5: Typical free-surface profile for $F = 0.3742$, $\epsilon = 5.0$ and $\tau^* = 0.3$. This solution is perturbed by solitary wave solution.
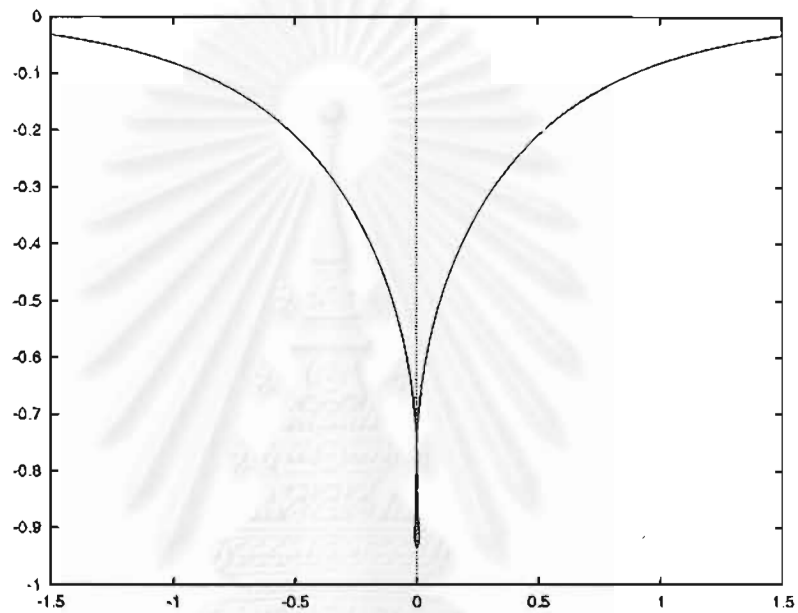
Figure 4.6: Typical free-surface profile in the case of approaching a limiting configuration with trapped bubble when $F = 0.2345$, $\epsilon = 0.0$ and $\tau^* = 0.3$.
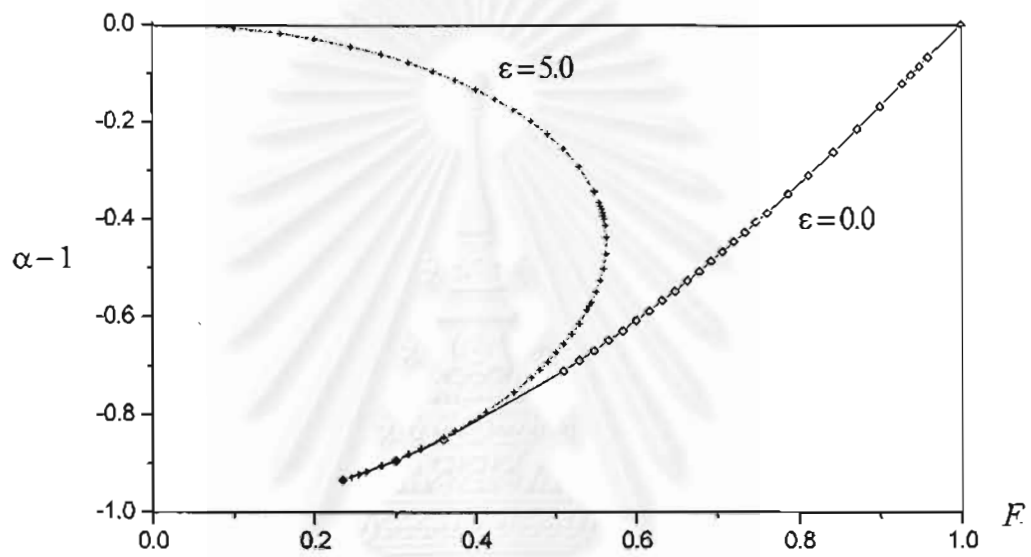
Figure 4.7: Plot of $\alpha - 1$ versus F when $\tau^* = 0.3$ for two values of ϵ : (i)$\epsilon = 0.0$ is represented by solid line and (ii) $\epsilon = 5.0$ is represented by dot-dash line.
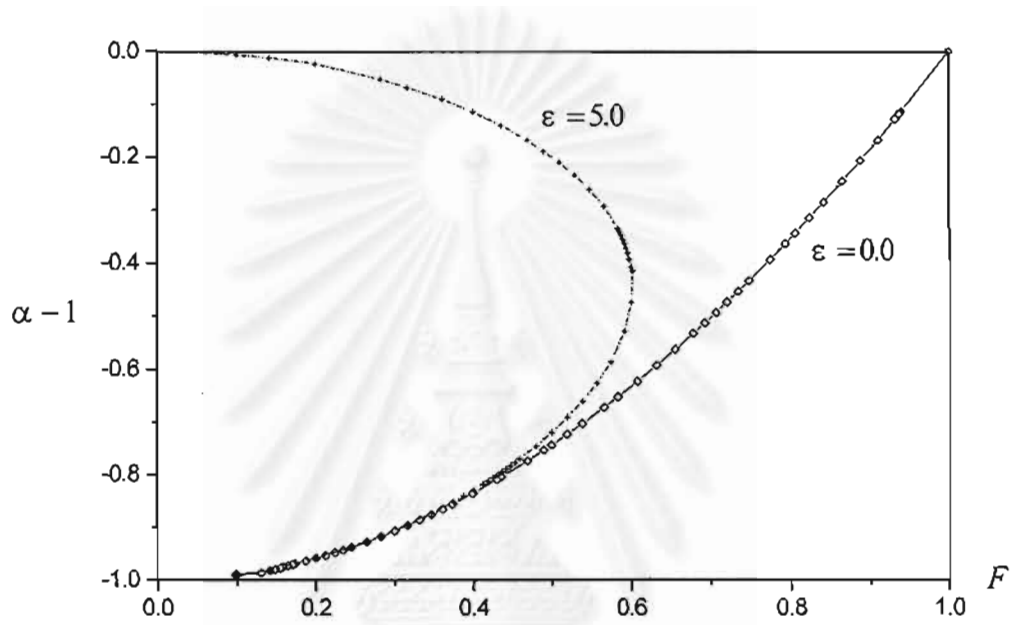
Figure 4.8: Plot of $\alpha - 1$ versus F when $\tau^* = 0.5$ for two values of ϵ : (i)$\epsilon = 0.0$ is represented by solid line and (ii) $\epsilon = 5.0$ is represented by dot-dash line.
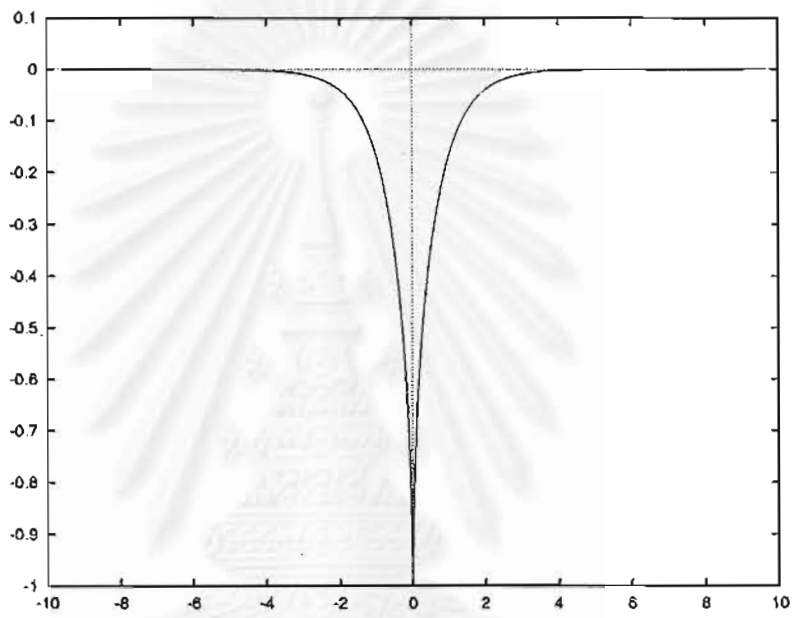
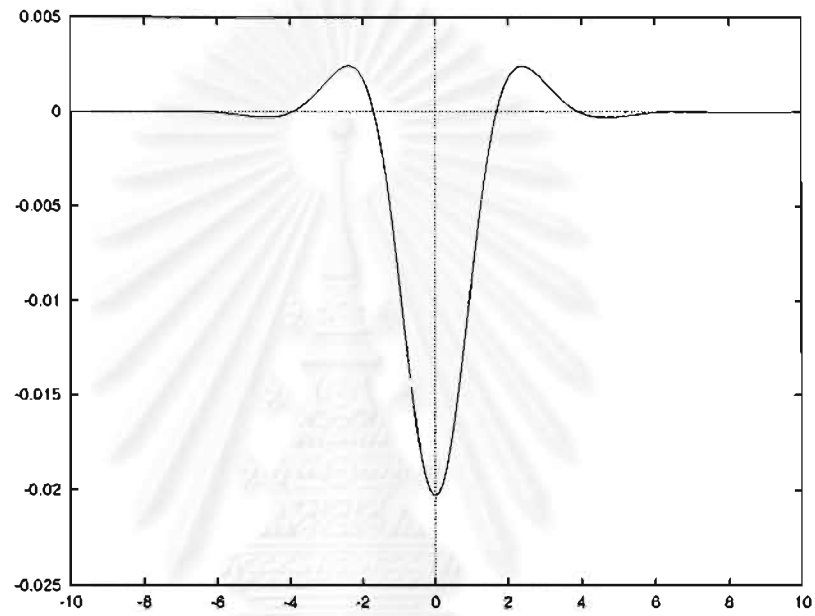Figure 4.9: Typical free-surface profile for $F = 0.0977$, $\epsilon = 0.0$ and $\tau^* = 0.5$.

Figure 4.10: Typical free-surface profile for $F = 0.9380$, $\epsilon = 0.01$ and $\tau^* = 0.25$.
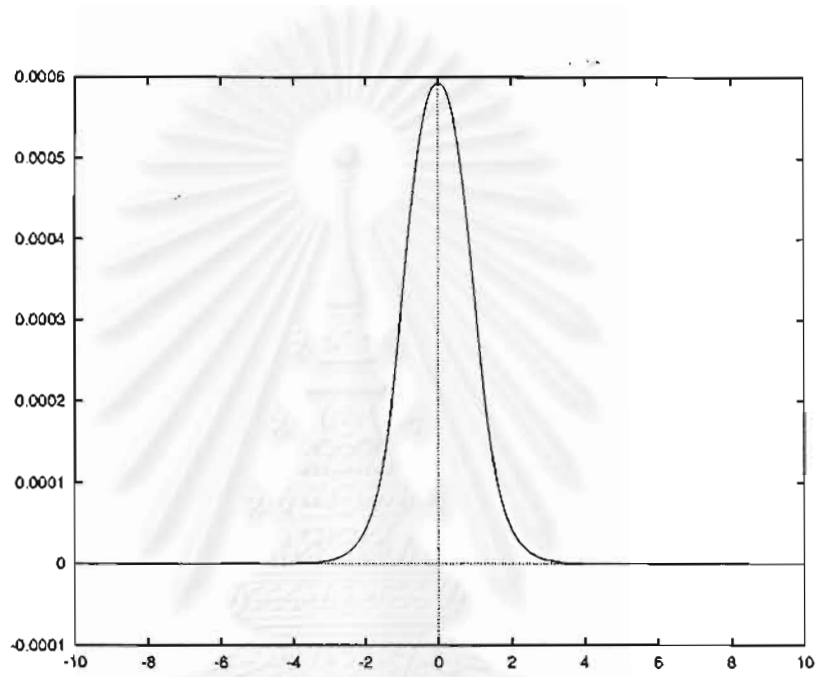
Figure 4.11: Typical free-surface profile for $F = 0.50$, $\epsilon = -0.01$ and $\tau^* = 0.25$.
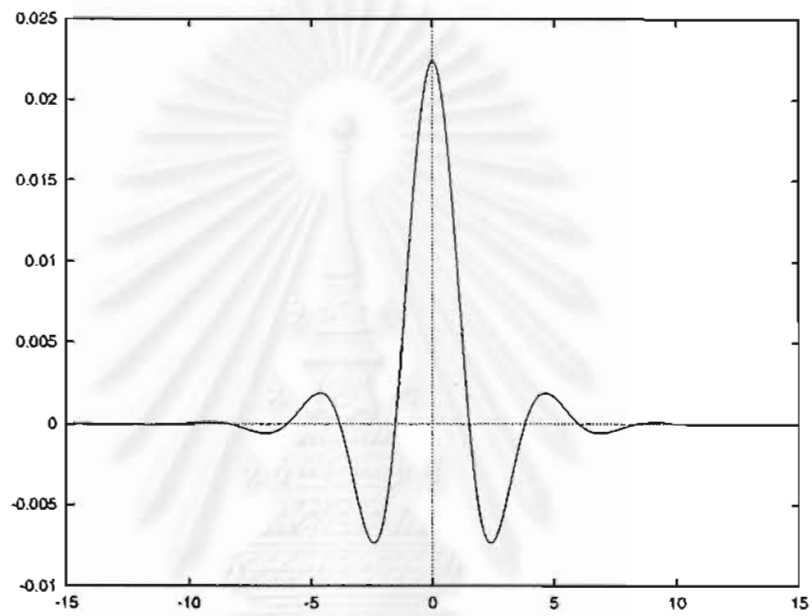
Figure 4.12: Typical free-surface profile for $F = 0.9592$, $\epsilon = -0.01$ and $\tau^* = 0.25$.

References

C. Von Kerczek and Nils Salvesen. Nonlinear free-surface effects-the dependence on Froude number. Proc. 2nd Int. Conf. On Numerical Ship Hydrodynamics Berkeley, 1977 : 292-300.

H. Lamb. Hydrodynamics. New York : Dover Publications, 1945.

J. Asavanant and J.M. Vanden-Broeck. Free-surface flows past a surface-piercing object of finite length. Journal of Fluid Mechanics 273, 1994 : 109-124.

J.K. Hunter and J.M. Vanden-Broeck. Solitary and periodic gravity-capillary waves of finite amplitude. Journal of Fluid Mechanics 134, 1983 : 205-219.

J.M. Vanden-Broeck. Numerical calculations of the free-surface flow under a sluice gate. Journal of Fluid Mechanics 330, 1997 : 339-349.

J.M. Vanden-Broeck and F. Dias. Gravity-capillary solitary waves in water of infinite depth and related free-surface flows. Journal of Fluid Mechanics 240, 1992 : 549-557.

L.K. Forbes and L.W. Schwartz. Free-surface flow over a semicircular obstruction. Journal of Fluid Mechanics 14, 1982 : 299-314.

L.W. Schwartz. Nonlinear solution for an applied overpressure on a moving stream. Journal of Engineering Mathematics 12, 1981 : 147-156.

Appendix

Appendix

Monàcella (1961) proved that a singularity in the Cauchy principal value integrals can be ignored in the numerical integration. This is achieved by spacing the mesh points symmetrically with respect to the pole. We show here by using the trapezoidal rule to compute the Cauchy principal value integral. We can also use the Simpson's rule to approximate such integral.

Let f be a continuous function. We approximate the integral of f over a finite interval $[a, b]$ by partitioning $[a, b]$ into N subintervals with $t_0 = a$ and $t_N = b$. Thus

$$\int_a^b f(t)dt \approx \sum_{i=0}^N f(t_i)W_i. \tag{1}$$

Here $h = (b-a)/N$ and

$$W_i = \begin{cases} \frac{h}{2} & , i = 0 \text{ and } N \\ h & , \text{ otherwise.} \end{cases} \tag{2}$$

We consider a function $\frac{f(t)}{t-x}$ with $f(x) \neq 0$ and $x \in (a, b)$. The integral of $\frac{f(t)}{t-x}$ over the variable t is of Cauchy principal value form. For any $\epsilon > 0$, we can write this integral as

$$\int_a^b \frac{f(t)}{t-x}dt = \lim_{\epsilon \to 0}\left[\int_a^{x-\epsilon} \frac{f(t)}{t-x}dt + \int_{x+\epsilon}^b \frac{f(t)}{t-x}dt\right]. \tag{3}$$

To compute this integral, we rewrite the integral on the left hand side of (3) as

$$\int_a^b \frac{f(t)}{t-x}dt = \int_a^b \frac{f(t)-f(x)}{t-x}dt + f(x)\int_a^b \frac{1}{t-x}dt. \tag{4}$$

Next we consider $N+1$ equally spaced mesh point $t_i, i = 0, ..., N$. Thus x is the midpoint between t_i and t_{i+1} for $i = 0, 1, ..., N-1$. There are two possible cases to be taken into account: (i) $x = (b-a)/2$ and (ii) $x \neq (b-a)/2$.

Case (i) $x = (b - a)/2$.

It can easily be shown that $\int_a^b \frac{dt}{t-x} = 0$. Thus (4) becomes

$$\int_a^b \frac{f(t)}{t-x} dt = \int_a^b \frac{f(t) - f(x)}{t-x} dt. \qquad (5)$$

Using the trapezoidal rule, we approximate the integral on the right hand side of (5) by

$$\int_a^b \frac{f(t)}{t-x} dt \approx \sum_{i=0}^N \frac{f(t_i) - f(x)}{t_i - x} W_i$$

$$= \sum_{i=0}^N \frac{f(t_i)}{t_i - x} W_i - f(x) \sum_{i=0}^N \frac{W_i}{t_i - x}$$

$$= \sum_{i=0}^N \frac{f(t_i)}{t_i - x} W_i. \qquad (6)$$

Here W_i and h are defined as in (1) and $\sum_{i=0}^N \frac{W_i}{t_i - x} = 0$ because x is midpoint of the interval $[a, b]$. Equation (6) suggests that the Cauchy principle value integral can be approximated as if it were an ordinary integral.

Case (ii) $x \neq (b - a)/2$.

Assuming that x is a midpoint on any interval $[c, d] \subset [a, b]$. We now rewrite (3) as

$$\int_a^b \frac{f(t)}{t-x} dt = \int_a^c \frac{f(t)}{t-x} dt + \int_c^d \frac{f(t)}{t-x} dt + \int_d^b \frac{f(t)}{t-x} dt \qquad (7)$$

The first and third integrals on the right hand side of (7) are not Cauchy principal values. Thus they can be approximated by the trapezoidal rule. The second integral is a Cauchy principle value with x as a midpoint of the interval $[c, d]$. The discussion in case(i) shows that it can also be evaluated by the trapezoidal rule. Therefore

$$\int_a^b \frac{f(t)}{t-x} dt \approx \sum_{i=0}^N \frac{f(t_i)}{t_i - x} W_i$$

Which is the same as (6). Thus, the singularity is subtracted from the Cauchy principal value integral leaving nonsingular integrals to evaluate as claimed.

Curriculum Vitae

Montri Maleewong was born in January 21, 1975. He received a bachelor degree in Mathematics from the Department of Mathematics, Faculty of Science, Chulalongkorn University in 1996. He is interested in ground water modeling and well-hydraulic and Computational Fluid Dynamics.